

1

2 **A multiscale modelling framework of coastal flooding events for** 3 **global to local flood hazard assessments**

4 Irene Benito¹, Jeroen C.J.H. Aerts^{1,2}, Philip J. Ward^{1,2}, Dirk Eilander^{1,2}, and Sanne Muis^{1,2}

5 ¹Institute for Environmental Studies (IVM), Vrije Universiteit Amsterdam, The Netherlands.

6 ²Deltares, Delft, The Netherlands.

7 *Correspondence to:* Irene Benito (i.benito.lazaro@vu.nl)

8 **Abstract.** Tropical and extratropical cyclones, which can cause coastal flooding, are among the most devastating natural
9 hazards. Understanding ~~better~~ coastal flood risk ~~better~~ can help to reduce their potential impacts. Global flood models play a
10 key role in this process. In recent years, global models and methods for flood hazard simulation have improved, but they still
11 present limitations to provide actionable information at local scales. One notable limitation is the insufficient resolution of
12 global models to accurately capture the complexities of storms and topography of specific regions. Additionally, most large-
13 scale hazard assessments tend to focus solely on either water level simulations or overland flooding, often relying on static
14 flood modelling approaches. In order to address some of those limitation~~In this study, we introduce we present the~~ MOSAIC
15 modelling framework, a flexible Python-based, – a novel modelling – framework designed that couples to dynamically
16 simulated dynamic both water levels and overland flood models coastal flooding events. We use MOSAIC to simulate three
17 historical storm events with the aim of assessing the effects of resolution in global models. MOSAIC’s flexibility allows for
18 the adjustment of both temporal and spatial model resolutions. Furthermore, its multiscale modelling approach allows to
19 automatically generate and nest high-resolution local models within a coarser global model. This approach seeks to generate
20 more accurate water levels, thereby enhancing coastal boundary conditions for dynamic flood modelling. Our findings indicate
21 that the importance of model refinements is linked to the topography of the study area and the storm characteristics. For
22 instance, refining temporal output resolution has a significant impact on small and rapidly intensifying tropical cyclones, but
23 is less critical for extratropical cyclones. Additionally, the refinement of spatial output locations is particularly relevant in
24 regions where water levels exhibit high spatial heterogeneity along the coast. In regions with complex topographies, grid
25 refinement and higher-resolution bathymetry play a more significant role. While the validation from this study does not
26 conclusively demonstrate that a specific refinement consistently yields better results, MOSAIC serves as a valuable resource
27 for users to explore optimal settings tailored to their case studies and regions of interest, providing~~MOSAIC follows a~~
28 multiscale modelling approach in which local models with high resolution are nested within a coarser large-scale model to
29 obtain higher-resolution water levels and provide better coastal boundary conditions for dynamic flood modelling. To
30 demonstrate the capabilities of MOSAIC we simulate three historical storm events. To merit the potential of MOSAIC’s
31 multiscale modelling approach we perform a sensitivity analysis. Our findings indicate that various model refinements
32 influence the simulation of total water levels and flood depths. The degree of importance of each refinement is linked to the
33 local topography of the study area, the spatial heterogeneity of the water levels and the storm characteristics. MOSAIC provides
34 a bridge between fully global and fully local modelling approaches, paving the way towards more actionable large-scale flood
35 risk assessments.

36 **1 Introduction**

37 Coastal flood events can have devastating impacts on societies, economies, and the environment when affecting densely
38 populated and low-lying coastal areas (Wadey et al., 2015). Tropical cyclones (TCs) and extratropical cyclones (ETCs) are the

39 cause of the most severe coastal flooding events (Douris et al., 2021; Dullaart et al., 2021; Haigh et al., 2016; UNDRR, 2020;
40 Wahl et al., 2017). For example, Hurricane Harvey, in 2017, is one of the costliest storms in the United States' history, with
41 an estimated damage of \$125 billion. Typhoon Imai, in Mozambique 2019, caused around 600 deaths and economic damages
42 of \$770 million (Nhamo and Chikodzi, 2021; Sebastian et al., 2021). In 1953, an ETC was the cause of the most severe coastal
43 flood event in Northwest Europe, resulting in more than 2000 deaths (Wadey et al., 2015). More recently, in 2010, ETC
44 Xynthia hit the Atlantic coast of France, causing 47 deaths and €1.2 billion economic damages (CGEDD, 2010).

45 Coastal flood events are driven by extreme sea levels, resulting from a combination of mean sea level variations, tides, storm
46 surges and waves (Kirezci et al., 2020; Marcos et al., 2019; Vousdoukas et al., 2018a, 2017; Wahl, 2017). In recent years,
47 several studies have applied global hydrodynamic models to simulate coastal water levels (Dullaart et al., 2021; Muis et al.,
48 2016; Pringle et al., 2021; Vousdoukas et al., 2016a; Wang and Bernier, 2023). Subsequently, these water levels have been
49 used to derive extreme water level values [for various return periods](#). These extreme water levels have then been used as input
50 into global overland flood models, and the resulting flood hazard maps have been used to assess flood exposure and risk
51 (Vousdoukas et al., 2016b). While these global studies have greatly improved our understanding of large-scale coastal flood
52 risks, they do not yet have the accuracy to provide actionable information about coastal flood events at local scales.

53 The accuracy of large-scale hazard assessments is limited by several factors related to the quality of the input data and
54 assumptions underlying the modelling approaches. Until now, the vast majority of large-scale hazard assessments have
55 primarily concentrated on either modelling extreme water levels or overland floods. However, each model component has its
56 own limitations. We identify here [two–three](#) main methodological limitations of large-scale hazard assessments. First,
57 [bathymetry and coastal geometry strongly influences extreme sea levels](#) (Bloemendaal et al., 2019; Dullaart et al., 2020; Mori
58 et al., 2014; Woodruff et al., 2023), with large variability at local scale. Consequently, in regions with complex morphologies,
59 such as estuaries, semi-enclosed bays or barrier systems, global models lack the resolution required to accurately resolve the
60 extreme sea levels (Bunya et al., 2010; Dietrich et al., 2010). Grid refinement and nesting of local high-resolution models
61 within coarser global models can result in improved coastal boundary conditions. ~~(Pelupessy et al., (2017) used a similar~~
62 [multiscale approach to obtain realistic boundary conditions by nesting a global circulation model and a high-resolution](#)
63 [barotropic model](#). Second, [the accuracy of input datasets such as the meteorological forcing and the bathymetry can have large](#)
64 [influence on the total water levels. Coarse meteorological forcings – both in terms of spatial and temporal resolution – might](#)
65 [not be able to capture the resolution necessary to resolve intense storms is often might lacks not be able to capture t, while](#)
66 [errors in the bathymetric datasets can result in changes will propagate to the modelling of in-storm surge levels](#) (Bloemendaal
67 et al., 2019; Dullaart et al., 2020).; Third, coastal flooding is a dynamic process where flood duration and physical [processes](#)
68 play a key role. However, [given](#) the high computational costs associated with using hydrodynamic flood models, [their use has](#)
69 [been limited to local application. for large-scale hazard assessments have limited m](#) Most large-scale hazard assessments [have](#)
70 [used to](#) static flood modelling methods, which neglect [the flood dynamics of flooding events for large scales](#) (Hinkel et al.,
71 2014; Muis et al., 2016; Ramirez et al., 2016; Vafeidis et al., 2019; Vousdoukas et al., 2016b). ~~Consequently, to date the use~~
72 [of hydrodynamic models has been mainly limited to local applications. Additionally, large-scale hazard assessments typically](#)
73 [focus on a single flood driver](#) (Tiggeloven et al., 2020; Vousdoukas et al., 2018b; Ward et al., 2020). ~~However, TC and ETC~~
74 [events often produce precipitation, river discharge, storm surges and waves, all of which can contribute to flooding. When](#)
75 [these drivers occur in combinations, they can significantly amplify flood hazards and risks. For instance, recent research](#)
76 [showed that storm surge exacerbates fluvial flooding at global scale](#) (Eilander et al., 2020). ~~Few studies have analysed the~~
77 [effects and interactions of multiple flood drivers. While \(Bates et al., \(2021\) performed a combined risk assessment of fluvial,](#)
78 [pluvial and coastal flooding for the continental USA. \(Eilander et al., \(2023\) introduced the first globally-applicable compound](#)
79 [flood modelling framework that accounts for precipitation, river discharge and storm tides \(Eilander et al., 2023\). However,](#)
80 [the inclusion of waves dynamically in large-scale assessments and the interactions between flood drivers remains a challenge.](#)

In this study, we introduce the MOSAIC (MOdelling Sea Level And Inundation for Cyclones) modelling framework with the aim of providing a flexible Python-based modelling framework that allows to dynamically simulate TC and ETC water levels and coastal flooding events. To address these two main limitations, we introduce the MOSAIC (MOdelling Sea Level And Inundation for Cyclones) modelling framework. MOSAIC is a flexible Python-based modelling framework designed to dynamically simulate TC and ETC coastal flooding events. To enhance analyse the effects of the model accuracy resolution in complex regions, MOSAIC applies a multiscale modelling approach in which local models with high-resolution (~45 m to 25 km) are nested within a large-scale model with a coarser resolution (~2.5 km to 25 km). To enable hydrodynamic flood modelling, MOSAIC couples two main-existing modelling approaches: (1) to simulate water levels generated from storm surges and tides at global to local scale it couples the hydrodynamic Global Tide and Surge Model (GTSM) and Delft3D Flexible Mesh software; and (2) to dynamically simulate overland flooding at local scale it couples the simulated water levels with the Super-Fast INunadation of CoastS model (SFINCS). We use a reproducible approach that is globally applicable and that can automatically generate local Delft3D Flexible Mesh models as well as local SFINCS models. In this study, we showcase the potential of the MOSAIC framework by applying it to three case studies where large storm surges caused catastrophic flooding events, namely historical storm events TC Irma, TC Haiyan, and ETC Xynthia (see Figure 1: (Bertin et al., 2012; Cangialosi et al., 2018; Lapidez et al., 2015). For each of these storms, we simulate the coastal water levels and flood depths. Moreover, we perform a sensitivity analysis of different modelling settings with the goal of benchmarking model configurations with different present the potential merits of the multiscale approach resolutions.

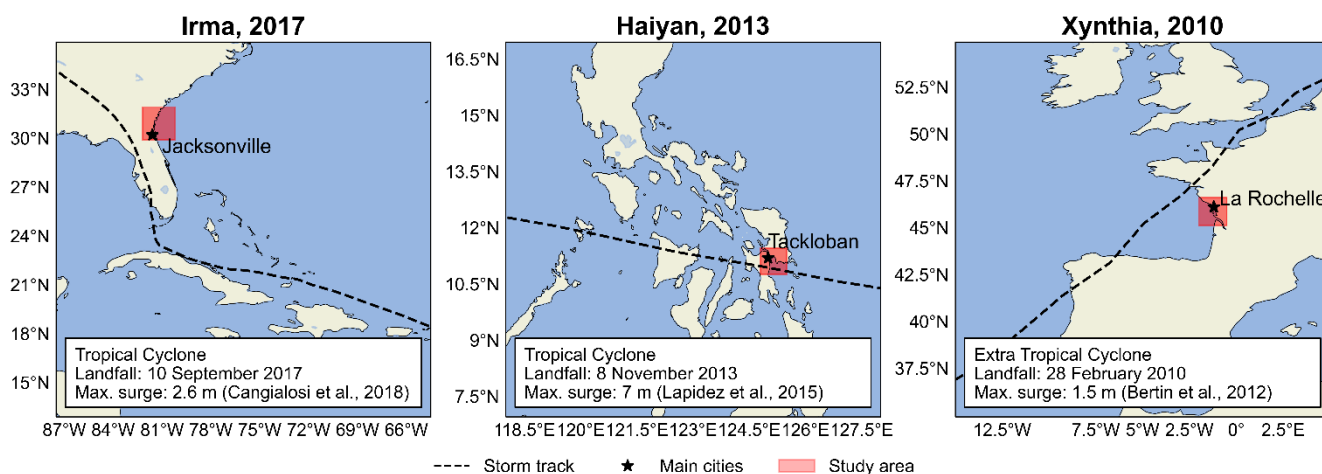


Figure 1. Case studies analysed on this paper. Left: Tropical cyclone Irma; middle: Tropical cyclone Haiyan; right: Extratropical cyclone Xynthia. The red area indicates the modelling domain of the flood analysis.

2 The MOSAIC modelling framework

The MOSAIC modelling framework, shown in Fig. 22, is a Python-based framework that integrates different packages, models and software. It consists of two main components: (1) the simulation of global coastal boundary conditions with the Global Tide and Surge Model (GTSM) (Section 2.1), including the dynamic downscaling with a local high-resolution model (Section 2.1.3); and (2) the overland flood hazard simulations using the SFINCS model (Section 2.2). Python scripts that enable adjustments to the GTSM settings are used to generate different model configurations. For the flood hazard simulations, MOSAIC uses the Hydro Model Tools (HydroMT) to prepare and postprocess SFINCS model input- and output data.

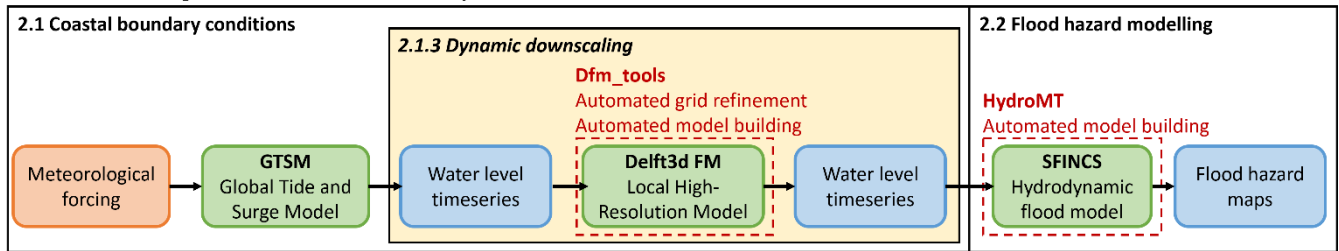


Figure 2. Flowchart showing the input (in orange), models (in green), outputs (in blue), Python packages (in red) and the optional dynamic downscaling feature (in yellow) of MOSAIC.

2.1 Derivation of coastal boundary conditions

2.1.1 Meteorological forcing

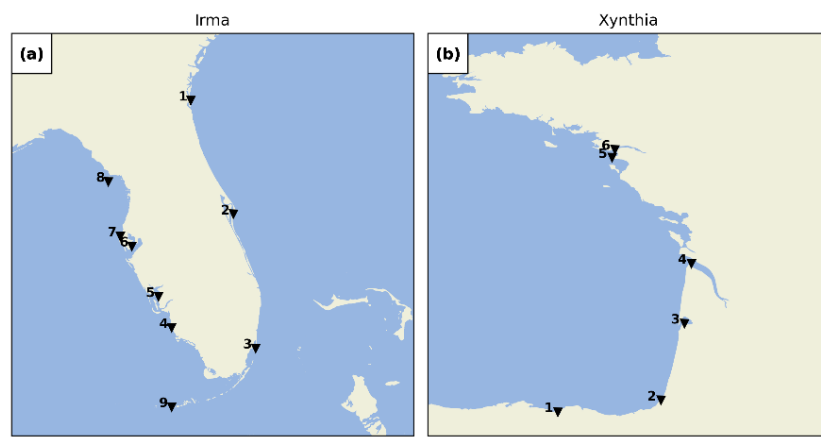
The meteorological forcing datasets used in this study vary per storm type. We force For ETC Xynthia and TC Irma, we use events with mean sea level pressure and 10 m meridional and zonal wind components from the ERA5 re-analysis dataset at a horizontal resolution of 0.25 degrees and 1 hour temporal resolution (Hersbach et al., 2019). Because TC Haiyan is not well resolved in ERA5 (see Fig. A1), we force TC events with use pressure and wind from tropical cyclone track data merged with mean sea level pressure and wind components from ERA5. The wind and pressure from tropical cyclone track data are retrieved from the National Hurricane Center from NOAA and the Joint Typhoon Warning Center at 6 hourly intervals (Naval Meteorology and Oceanography Command, 2022) and are converted to a polar grid with 36 radial bins, 375 arcs and a radius of 500-350 km using the Holland parametric wind model (Holland et al., 2010). Following the methodology of (Dullaart et al., (2021) and Lin and Chavas, (2012), we apply a counter-clockwise rotation angle of $\beta = 20^\circ$ and set the storm translation to surface background wind reduction factor at $\alpha = 0.55$. Additionally, we use an empirical surface wind reduction factor (SWRF) of 0.85 (Batts et al., 1980), and convert 1-minute average winds to 10-minute averages using a factor of 0.915 (Harper et al., 2010). The Holland model's output provides a file that defines a polar grid containing pressure and wind fields. To extend the pressure and wind fields beyond the Holland model's defined TC boundary, within GTSM we linearly interpolate these fields on the outermost 75% (i.e. 75% of 350 km) to the edge to align with the ERA5 background data. The pressure and wind fields derived from track data are linearly interpolated from their outermost 33% with the ERA5 data in the background (Deltares, 2024).

2.1.2 Global storm surge and tide model

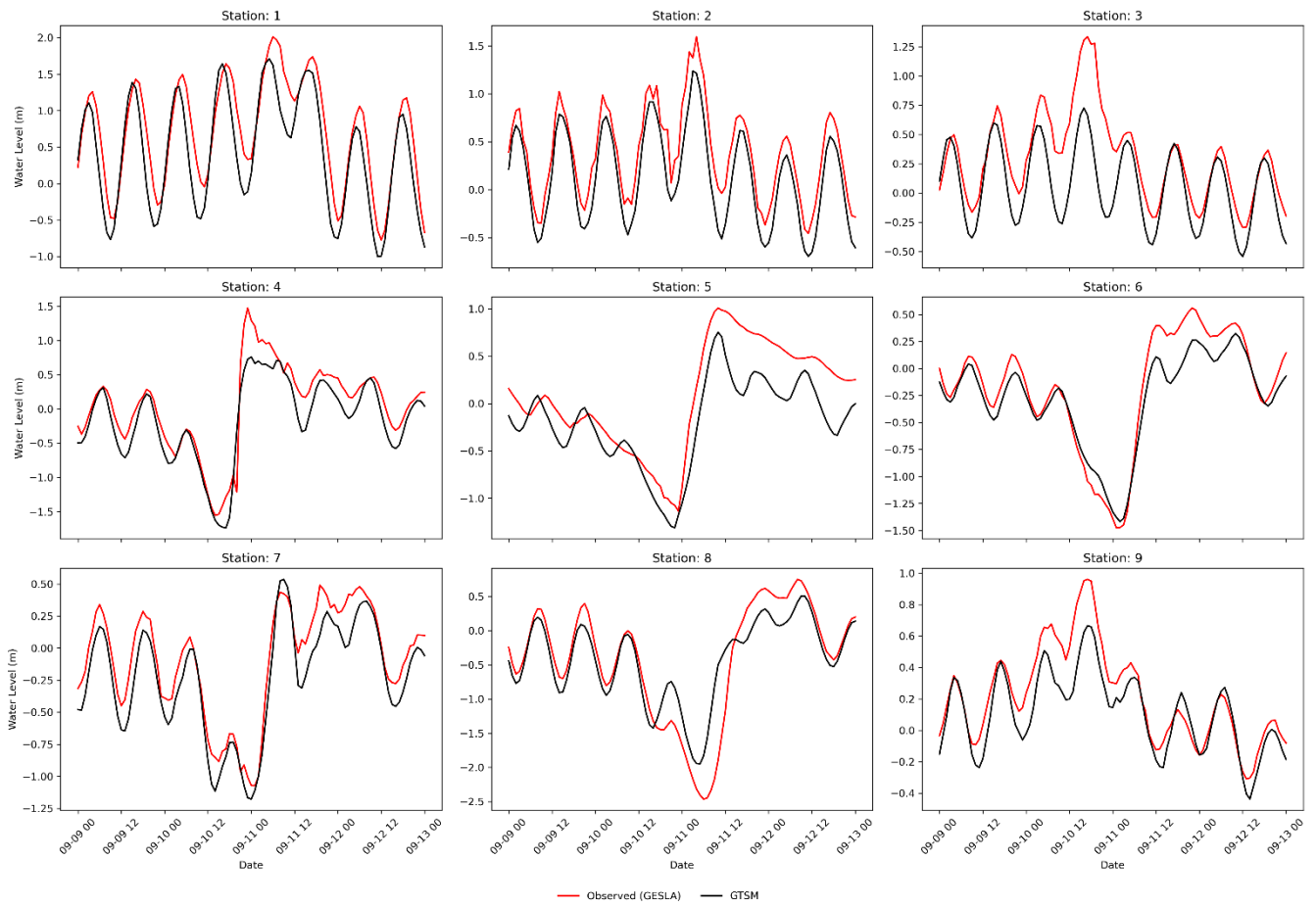
MOSAIC uses GTSMv4.3.10 to simulate total water levels resulting from tides and storm surges, ignoring baroclinic and wave contributions. GTSM is a global depth-averaged hydrodynamic model based on Delft3d Flexible Mesh (Kernkamp et al., 2011). It has a spatially-varying resolution of 25 km deep in the ocean and 2.5 km along the coasts (1.25 km for Europe) (Dullaart et al., 2020; Muis et al., 2020). The spatially-varying resolution makes it computationally efficient for simulating water levels at large scales. The bathymetry in the model is the 15 arcseconds resolution EMODnet bathymetry dataset for Europe (Consortium EMODnet Bathymetry, 2018), and the 30 arcseconds General Bathymetric Chart of Oceans 2019 dataset for the rest of the globe (GEBCO, 2014). Tides are generated internally with tide generating forces, while storm surges originate from external forcing with pressure and fields (Section 2.1.1; Muis et al., 2020). GTSM has been successfully validated using different meteorological datasets and has been shown to provide accurate extreme sea levels (Dullaart et al., 2020; Muis et al., 2020, 2016). Version 4.1 is a calibrated version of the model with also improved parameterizations for internal tides and bottom friction coefficient (Deltares, 2021; Wang et al., 2022). GTSM provides as output water level timeseries over a grid in the ocean and for locations along every ~5 km of the coast.

To validate the coastal component of our modelling framework, we compare total water levels from GTSM against observed total water levels from tide gauge stations of the Global Extreme Sea Level Analysis (GESLA) dataset (Haigh et al., 2023).

188 This comparison is made for case studies where the GTSM output locations are found nearby tide gauge stations from GESLA
189 (see Figure 3). GTSM output is referenced to mean sea level (MSL). We reference the GESLA water levels to the MSL by
190 removing the annual average water level for each year, and subsequently removing the mean over the 1985-2005 period from
191 the de-trended time series. To assess the accuracy of GTSM, we calculate the Pearson's correlation coefficient and the root
192 mean-squared error (RMSE; see Table A1). Figure 4 and Fig. 5 show the time series of total water levels at different tide gauge
193 stations during for the periods surrounding the landfall of TC Irma and ETC Xynthia, respectively. These figures compare the
194 GTSM-simulated total water levels with the observed data. The Pearson's correlation between the GTSM-simulated and
195 observed total water levels is high strong for both events, indicating showing a good agreement simulation of the timeseries
196 patterns over time. For TC Irma, the average correlation across the nine stations is 0.93 with a standard deviation of 0.06 m.
197 For ETC Xynthia, the average correlation across the six stations is 1.00 with a standard deviation of 0.01. Additionally, TC
198 Irma has a RMSE of 0.28 m with a standard deviation of 0.09 m, and ETC Xynthia has a RMSE of 0.22 m with a standard
199 deviation of 0.08 m. This shows that while there are some minor differences between the GTSM simulations and observations,
200 generally there is a good agreement the predictions are generally accurate and reliable.

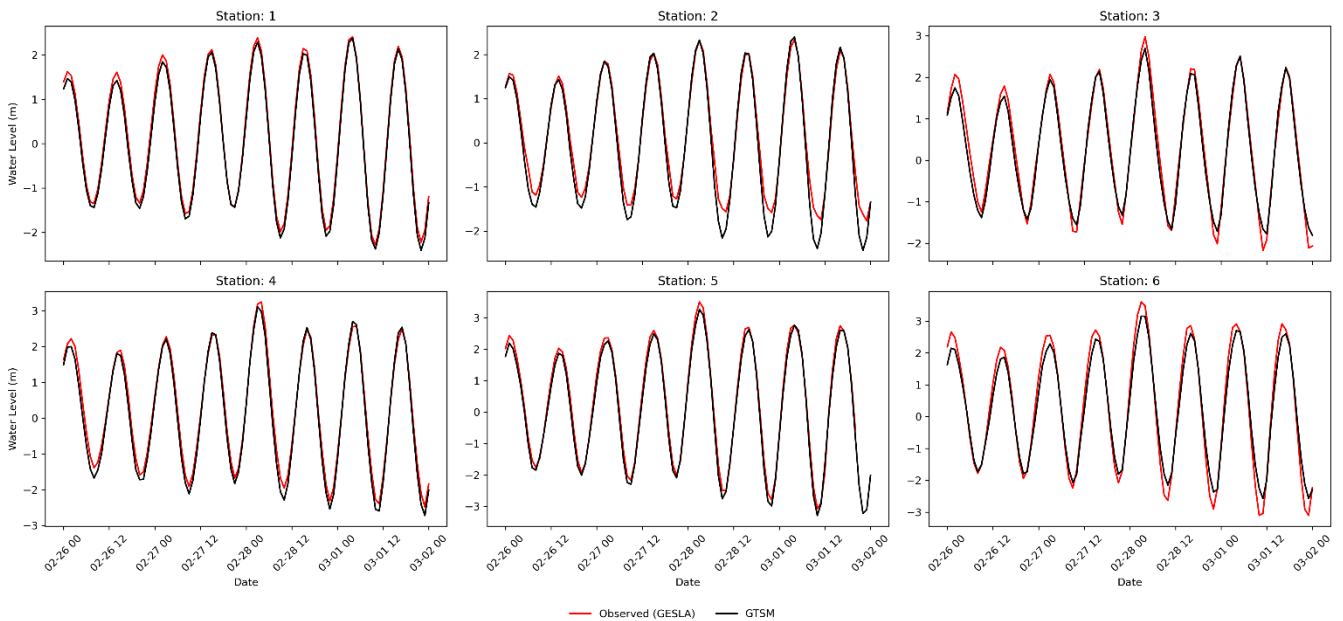


201
202 **Figure 3. GESLA tide gauge stations for the case studies Irma (panel a) and Xynthia (panel b).**



203

204 **Figure 4. Validation of total water levels for the case study Irma, for the nine tide gauge stations depicted in Figure 3.**



205

206 **Figure 5. Validation of total water levels for the case study Xynthia, for the six tide gauge stations depicted in Figure 3.**

207 **2.1.3 Dynamic downscaling**

208 The dynamic downscaling within MOSAIC consists of two parts. First, MOSAIC generates a local high-resolution model with
 209 Delft3D Flexible Mesh using the Python package dfm_tools (Veenstra, 2024). Dfm_tools allows to automatically create a
 210 local modelling grid with a spatially-varying resolution based on the specified maximum and minimum grid cell sizes as well

211 as the Courant's number derived from the bathymetry data [provided](#) (Veenstra, 2024). [The bathymetry of the local model can](#)
212 [be updated by interpolating a new bathymetric dataset into the newly generated grid.](#) The settings to automatically generate
213 the local high-resolution models used in this study can be found in Section 2.3. Second, MOSAIC uses an offline coupling
214 approach to nest the local Delft3D Flexible Mesh model within GTSM. [A Python script is used to first identify the boundaries](#)
215 [of the local Delft3D Flexible Mesh model. These boundaries are then used to determine the specific locations where GTSM](#)
216 [output should be extracted. Subsequently,](#) GTSM provides the water level timeseries at the ~~model~~-boundaries of the local
217 model. ~~Then~~ Finally, the local high-resolution model is executed using the water levels derived from GTSM as forcing input,
218 together with the same meteorological forcing as for GTSM.

219 2.2 Hydrodynamic flood hazard modelling setup

220 MOSAIC uses the Super-Fast INundation of CoastS (SFINCS) model to simulate overland storm surge flood depths. SFINCS
221 is a reduced-physics hydrodynamic model developed for a more computationally efficient dynamic flooding approach than
222 full shallow water equation models (Leijnse et al., 2021). It solves simplified equations of mass and momentum, similar to the
223 LISFLOOD-FP model (Bates et al., 2010). SFINCS has been successfully applied to model compound flooding for tropical
224 cyclone Irma in 2017 (Eilander et al., 2023; Leijnse et al., 2021). Its modelling output results in similar results to those from
225 full shallow water equation models, while reducing computational expenses by a factor of 100 (Leijnse et al., 2021). To speed
226 up the flood model simulations, we use the subgrid schematization from SFINCS for all the simulations (Leijnse et al., 2020).

227 For this study, we use GEBCO 2020 (15 arc seconds spatial resolution; (Weatherall et al., 2020)) [as input dataset for the](#)
228 [bathymetry](#) and ~~as input datasets the land elevation we use~~ FABDEM (30 m spatial resolution; (Hawker et al., 2022)) ~~as input~~
229 ~~dataset for the land elevation of TC Irma and Haiyan. Except for ETC Xynthia. For ETC Xynthia, there we use the 5 m~~
230 [resolution LiDAR-based DEM developed by the French National Geographic Institute \(IGN\) because it can represent better](#)
231 ~~represents dikes the flood protection measures present in the region, leading to better flood estimates than FABDEM (see Fig.~~
232 [A8\) as input datasets for the bathymetry and the land elevation respectively.](#) The spatially varying roughness coefficients used
233 within SFINCS are derived from the land use maps of the Copernicus Global Land Service (Buchhorn et al., 2020). Within
234 MOSAIC, SFINCS is coupled offline with water levels from GTSM at 1-hourly resolution for the default settings. The Mean
235 Dynamic Topography (DTU10MDT; (Andersen and Knudsen, 2009)) is used to convert the vertical reference of the water
236 levels from mean sea level to the EGM2008 geoid, ~~which is the datum of FABDEM.~~ The resulting flood hazard maps have a
237 resolution of 30 m.

238 To build the SFINCS models and couple them with GTSM, MOSAIC ~~makes uses of~~ the HydroMTv~~01.70.10~~ (Hydro Model
239 Tools) package (Eilander et al., 2023). HydroMT is an open-source Python package, which provides automated and
240 reproducible model building and analysis of results. HydroMT uses a modular approach in which datasets and model setup
241 ~~configurations~~ can easily be interchanged. In the MOSAIC framework presented in this paper, we take advantage of HydroMT
242 in several ways: (1) to automatically convert the forcing files from GTSM and the other input into the ~~ir relevant model specific~~
243 [input](#) format; (2) to easily build a ~~complete reproducible~~ SFINCS model; and (3) to perform the analysis of the ~~flood SFINCS~~
244 model output. [SFINCS is forced with GTSM water level timeseries at locations along every ~5 km of the coastline, and](#)
245 [provides as output water level timeseries for each grid cell. Finally, flood depth maps are derived from the maximum water](#)
246 [levels by subtracting the DEM.](#)

247 [To validate the hydrodynamic flood hazard modelling component of the modelling framework, we compare the modelled flood](#)
248 [extents with observed flood extents derived from field measurements. This comparison is done for Xynthia, the only case study](#)
249 [for which observed flood extent data are available \(Breilh et al., 2013; DDTM, 2011\). We measure the model skill using: \(1\)](#)
250 [the hit rate \(H\), defined as the flood area correctly simulated over the observed flooded area \(Eq \(1\)\); \(2\) the false-alarm ratio](#)
251 [\(F\), defined as the area wrongly simulated over the observed flooded area \(Eq \(2\)\); and \(3\) the critical success index \(C\),](#)

defined as the area correctly simulated to be flooded over the union of the observed and modelled flooded area (Eq (3)). Figure 6 shows the skill of the modelled maximum flood extents by SFINCS using the GTSM water levels output of the default GTSM configuration as a forcing. The hit rate is 0.78, correctly representing being the flooding in most regions, only underestimating it in regions further inland but underestimating. The false-alarm ratio of the model is 0.62. Flooding is overestimated in the north, likely due to the lack of flood protection measures included in the model that are present in reality in the region. The critical success index is 0.48, as a result of the areas well simulated and those over and underpredicted. While the performance of the flood model is negatively affected by the quality of the topography and the representation of local features such as dikes, we consider the performance sufficient for large-scale modelling and comparable to other studies such as (Ramirez et al., (2016) and; Vousdoukas et al., (2016b).

$$H = \frac{F_{\text{modelled}} \cap F_{\text{observed}}}{F_{\text{observed}}} \quad (1)$$

$$F = \frac{F_{\text{modelled}} / F_{\text{observed}}}{F_{\text{observed}}} \quad (2)$$

$$C = \frac{F_{\text{modelled}} \cap F_{\text{observed}}}{F_{\text{modelled}} \cup F_{\text{observed}}} \quad (3)$$

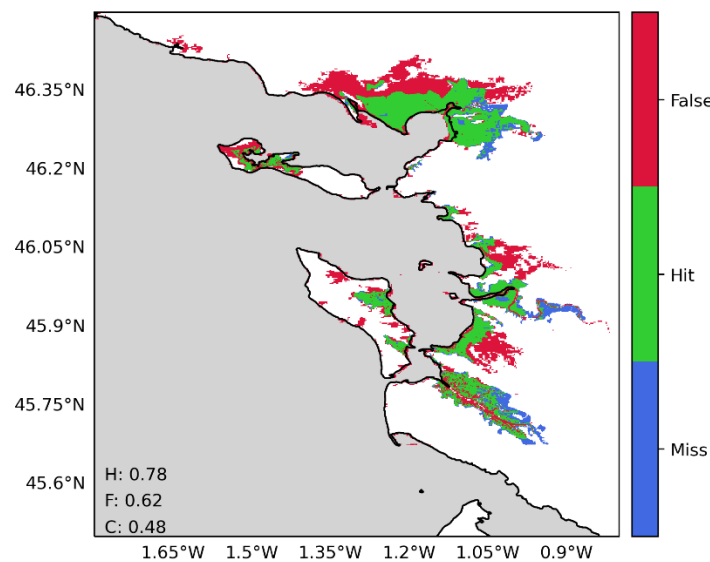


Figure 6. Validation of the flood hazard modelling component of the modelling framework for the case study Xynthia, using the water levels of the default configuration of GTSM as a forcing. The maps compare the modelled and observed maximum flood extents, where: green indicates flood areas correctly simulated; blue flood areas not simulated but observed; and red flood areas simulated but not observed. Performance indicators for the hit rate (H), false-alarm ratio (F) and critical success index (C) are shown in each panel.

2.3 Sensitivity analysis

Using the MOSAIC modelling framework, we analyse the effects of refining the resolution of GTSM on the simulated water levels and assess how these propagate into the results for the flood hazard simulated by SFINCS. As described in Table 1, we categorise model configurations in two distinct groups. The first group, which contains the global model configurations (G), includes the default model configuration (G1) and configurations that modify only the global GTSM model (G2 and G3). In this group, the refinements applied are: (1) the temporal output resolution, which is different than the implicitly calculated simulation timestep of GTSM, is refined from 1-hourly to 10-minute, allowing to capture more changes in water levels, including the peaks of the water levels (G2); and (2) the spatial output resolution is refined from locations along the coast every ~5 km to ~2 km, providing more coastal boundary conditions for the hydrodynamic flood hazard model (G3). The second

group, which contains the nested model configurations (N), includes those model configurations that use a nested local model within the global model GTSM by performing dynamic downscaling. These model configurations include: (1) the nesting of local high-resolution models with refined grids into GTSM (N1); and (2) the nesting of local high-resolution models with refined grids and updated bathymetry into GTSM (N2). Finally, we evaluate the combined effects of all these refinements through the “fully refined” configuration (N3), which integrates both the enhanced temporal and spatial resolutions as well as the nested high-resolution models and updated bathymetry. The validation of GTSM and SFINCS shows sufficient performance for all the model configurations from Table 1 and Fig. 7 (see Table A1 and Figs. A2, A3 and A9).

we define a fully refined model configuration by combining three different refinements that can lead to more accurate results than those for the default GTSM: (1) the temporal output resolution, which is different than the implicitly calculated timestep of GTSM, is refined from 1 hourly to 10-minute, allowing to capture more changes in water levels, including the peaks of the water levels; (2) the spatial output resolution is refined from locations along the coast every ~5 km to ~2 km, providing more coastal boundary conditions for the hydrodynamic flood hazard model; and (3) the dynamic downscaling is performed to nest local high-resolution models into GTSM, allowing to resolve better the water levels on areas with complex topographies. Subsequently, we compare the coastal water levels and flood depths of the “fully refined” against the results of the default configuration of GTSM. To understand how each of the three model refinements affect the output of the fully refined configuration, we also analyse the effects of each individual refinement against the results of the default configuration. These comparisons will provide insights in the potential merits of refining the global modelling approach and dynamic downscaling. Figure 3 provides a detailed overview of the different modelling configurations for the three case studies.

Table 1. GTSM model configurations used in the sensitivity analysis.

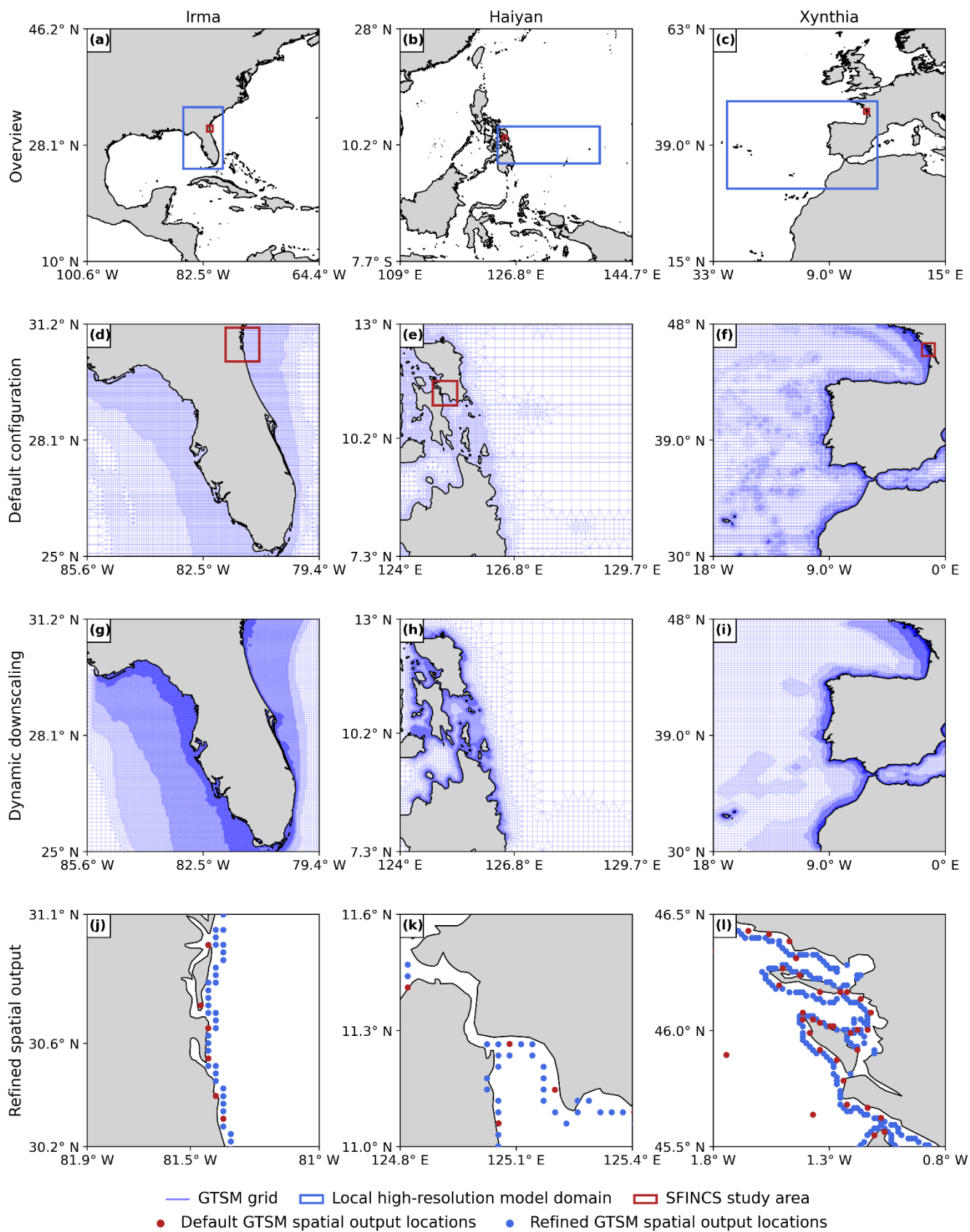
<u>Model configuration</u>	<u>Nomenclature</u>	<u>GTSM grid resolution</u>	<u>Bathymetry</u>	<u>Spatial output resolution</u>	<u>Temporal output resolution</u>
<u>Default configuration</u>	<u>G1</u>	<u>~25 to 2.5/1.25km</u>	<u>GEBCO201 9*</u>	<u>Original (~5 km)</u>	<u>1h</u>
<u>Refined temporal output resolution</u>	<u>G2</u>	<u>~25 to 2.5/1.25km</u>	<u>GEBCO201 9*</u>	<u>Original (~5 km)</u>	<u>10min</u>
<u>Refined spatial output</u>	<u>G3</u>	<u>~25 to 2.5/1.25km</u>	<u>GEBCO201 9*</u>	<u>Refined (~2 km)</u>	<u>1h</u>
<u>Dynamic downscaling (Refined grid)</u>	<u>N1</u>	<u>~25 to 0.45km</u>	<u>GEBCO201 9*</u>	<u>Original (~5 km)</u>	<u>1h**</u>
<u>Dynamic downscaling (Refined grid + Updated bathymetry)</u>	<u>N2</u>	<u>~25 to 0.45km</u>	<u>GEBCO202 3</u>	<u>Original (~5 km)</u>	<u>1h**</u>
<u>Fully refined configuration</u>	<u>N3</u>	<u>~25 to 0.45km</u>	<u>GEBCO202 3</u>	<u>Refined (~2 km)</u>	<u>10min**</u>
<u>Model configuration</u>		<u>GTSM grid resolution</u>	<u>Bathymetry</u>	<u>Spatial output resolution</u>	<u>Temporal output resolution</u>
<u>Default configuration</u>		<u>~25 to 2.5/1.25km</u>	<u>GEBCO2014*</u>	<u>Original</u>	<u>1h</u>

				(~5 km)	
Fully refined configuration	~25 to 0.45km	GEBCO2023	Refined (~2 km)		10min**
Refined temporal output resolution	~25 to 2.5/1.25km	GEBCO2014*	Original (~5 km)		10min
Refined spatial output	~25 to 2.5/1.25km	GEBCO2014*	Refined (~2 km)		1h
Dynamic Downscaling	~25 to 0.45km	GEBCO2023	Original (~5 km)		1h**

344 * EMODnet2018 for Europe ([Xynthia case study](#))

345 **[For the model configurations N1, N2 and N3](#) When applying dynamic downscaling, the temporal output resolution is also the temporal
346 resolution of the coupling between GTSM and the local high-resolution model.

347



348

349 **Figure 73.** Overview of the model domains for the local high-resolution model and SFINCS, for the three case studies (panels a, b,
 350 c); default GTSM grid zoomed in (d, e, f); local high-resolution model grid zoomed in (g, h, i) and; GTSM spatial output locations
 351 for the default configuration and the refined spatial output configuration, zoomed into the SFINCS study area (j, k, l). (Breith et al.,
 352 2013; DDTM, 2011)(Breith et al., 2013; DDTM, n.d.)

3 Sensitivity analysis of the model results

3.1 Multiscale storm surge modelling

Figure 8 panels a, e and i show the maximum water levels simulated by G1 for the three case studies, and depict the maximum observed water levels for various GESLA tide gauge stations. To understand the effect of each individual refinement in the maximum total water levels, Figure 8 presents the differences in maximum water levels between each refinement and the model configuration G1. Figure 9 presents the differences in maximum water levels between the fully refined model configuration N3 and the model configuration G1.

3.1.1 Effects of higher resolution on total water levels

Figure 8 panels b, f, j show that the refinement of To understand the contribution of each refinement in the maximum water level differences between the fully refined configuration and the default configuration, Fig. 5 presents the differences in maximum water levels between each refinement and the default configuration. Refining the temporal output resolution of GTSM from 1-hourly to the 10-minute intervals of G2 (Fig. 5 panels b, e, h) results in higher maximum water levels across the entire model domain for all three case studies. For TC Irma (Fig. 8 panel b), the sensitivity of the water levels to the temporal refinement is relatively small, up to less than 120 cm. The small effect of the temporal refinement for TC Irma can be observed as well in Table A1 and Fig. A2, where G1 and G2 present similar timeseries and performance coefficients when compared to observed water levels. Water levels increase due to the temporal output refinement mostly at the location of landfall, south of Florida, while near Jacksonville the water level changes are much smaller. The cause for this might be the fact that TC Irma did not directly pass over Jacksonville, therefore the storm surge generated in that region is mainly being driven by less intense outer winds that are less sensitive to changes in temporal resolution. For TC Haiyan (Fig. 8 Fig. 5 panel f), the sensitivity of the water levels is significant. Water levels increase due to the temporal refinement up to about 1.2 m along the coastlines where TC Haiyan made landfall, showing that 1-hourly resolution is too coarse to accurately capture the water level response. The cause for this might be that TC Haiyan had a rapid intensification, and when modelling water levels at 1-hourly resolution we might overlook the storm's peak, resulting in an underestimation of the maximum water levels. G2 however, can capture the peak of TC Haiyan more precisely (see Figs. A4 and A5). For ETC Xynthia (Fig. 8 Fig. 5 panel h), the sensitivity of the water levels to the temporal refinement is relatively small, less than 10 cm on average, and slightly higher in enclosed basins and estuaries near La Rochelle. The small changes in water levels for ETC Xynthia are likely due to the inherent characteristics of ETCs, which typically have larger dimensions, lower intensity, and a slower rate of intensification compared to TCs. This means that the changes in water levels can be well captured at a 1-hourly resolution. The small effect of the temporal refinement for ETC Xynthia can be observed as well in Table A1 and Fig. A3, where G1 and G2 present similar timeseries and performance coefficients when compared to observed water levels.

The model configuration G3, where Refining the spatial output resolution is refined, is not shown in Fig. 8 Fig. 5 because increasing the number of water level locations does not change the water level values themselves. However, this refinement becomes significant when these values are applied as coastal boundary conditions to SFINCS (see Section - 3.2.1), as a greater number of coastal boundary conditions offer additional information for the flood model.

3.1.2 Effects of dynamic downscaling with original bathymetry on total water levels

Figure 8 panels c, g, k show that the model configuration N1 results in significant changes in water levels for all case studies. The largest differences occur along the coasts, where the largest changes in model grid size resolution occur. For TC Irma (Fig. 8 panel c), the nesting of a local model at high-resolution with GEBCO2019 results in maximum water levels that are up to 0.3 m higher than G1 in the southwest of Florida, and up to 0.1 m lower in the southwest. These changes are caused by the refined grid resolution in those regions in comparison to G1, which allows us to better resolve complex topography around the barrier islands. Water levels for nine tide gauge stations along the coast indicate that while G1 underestimates the peak of TC Irma in most locations (Fig. A2, all stations but station 7), N1 simulates on average higher peaks, resulting sometimes in

overestimations (Fig. A2, station 9). Additionally, the performance of N1 is slightly better than G1 for six tide gauge stations (stations 1-6), as reflected in Table A1, which shows lower RMSE values. However, for stations 7-9, G1 shows slightly higher RMSE and Pearson's correlation. For TC Haiyan (Fig. 8 panel g), the differences in maximum water levels are up to 1 m higher than G1 near the landfall regions. These differences occur due to the refinement of the grid from 2.5 km to 45 m, which results in a significant increase in the number of model grid cells that define regions of shallow bathymetry, especially around the bay near Tacloban, resulting in a more detailed representation of water levels in that region. Thanks to the increase on grid cells, the strait north of Tacloban for N1 is defined with multiple grid cells in comparison to the two grid cell width of G1 (see Fig. A6). Therefore, in that region N1 allows us to better resolve the topography of the region, and water can travel more easily northwards. For ETC Xynthia (Fig. 8 panel k), the water levels from the nested local model at high-resolution are overall lower than water levels for the G1. Near La Rochelle, those water levels are up to 0.2 m lower. When comparing the performance of N1 with G1 (Table A1 and Fig. A3), both model configurations can predict the timeseries pattern well, with high Pearson's correlation coefficients. Overall, the RMSE for Xynthia is similar for most tide gauge stations, except for two stations located in the mouth of estuaries (stations 3 and 6).

Figure 5. Maximum water levels for the three case studies, for the default configuration (panels a, d, g). Difference between the maximum water level for each specific model configuration and the default configuration. Difference in water levels for the temporal output resolution refined configuration (panels b, e, h) and the dynamic downscaling configuration (panels c, f, i).

3.1.3 Effects of dynamic downscaling with updated bathymetry on total water levels

Figure 8 panels d, h, l show that the model configuration N2 Dynamic downscaling (Fig. 5 panels e, f, i) results in relatively large changes in the water levels for all the case studies. The largest differences occur along the coasts and provide figures similar to those from N1. For TC Irma (Fig. 8 5-panels -c), the nesting of a local model at high-resolution with updated GEBCO2023 bathymetry results in maximum water levels that are 0.35 m higher than the default configuration G1 in the south of Florida. Compared to N1, model configuration N2 provides slightly higher water levels south of Florida. Those differences come from differences between GEBCO2023 and GEBCO2019 in the region. N2 shows a similar performance to G1 and N1 across nine tide gauge stations (Table A1 and Fig. A2). Those differences might be due to changes in the bathymetric data from GEBCO2014 to GEBCO2023, which can resolve better the shallow regions around the landfall location and due to the grid refinement of the region near landfall, which provides more accuracy around the barrier islands, allowing to resolve better the water levels. Near Jacksonville, approximately 500 km distance from the landfall location, the difference in maximum water levels instead are approximately 0.1 m higher. For TC Haiyan (Fig. 8 5-panels f-h), the differences in maximum water levels are up to 1 m higher and lower than the default configuration near than G1 at the landfall regions. Compared to N1, N2 provides on average higher maximum water levels, except in the bay of Tacloban where N1 presents on average higher maximum water levels. These differences come from the differences in GEBCO2019 and GEBCO2023. These differences might occur due to the update in bathymetry, where certain areas are shallower and certain areas deeper for GEBCO2023 in comparison to the default GEBCO2014 dataset. Furthermore, the refinement in the grid from 2.5 km to 45 m results in a significant increase in the number of model grid cells that define regions of shallow bathymetry, especially around the bay near Tacloban, resulting in a more detailed resolution of water levels in that region. Thanks to the increase on grid cells, on the strait north of Tacloban GTSM is able to better resolve the water levels, and therefore, water can travel northwards. For ETC Xynthia (Fig. 8 5-panels l), the water levels from the nested local model at high-resolution with GEBCO2023 are lower overall than water levels for G1 the default configuration. Compared to N1, the model configuration N2 provides a similar pattern of water level decrease, however, the maximum water level reduction compared to G1 is slightly less than for N1. The performance of N2, as shown in Table A1 and Fig. A3, is comparable to that of G1 and N2, except at two tide gauge stations (station 3 and 6) where GEBCO2023 does not accurately capture the bathymetry of the river channels in the estuaries. In

contrast, EMODNET2018, the bathymetry used in model configurations N1 and N3, better resolves these details (see Fig. A7). Near La Rochelle, those water levels are approximately 0.3 m lower. The reason for this might be due to differences in the bathymetry in the region around La Rochelle, and due to the fact that the refined grid has more grid cells that resolve the water travelling through the estuaries in the region.

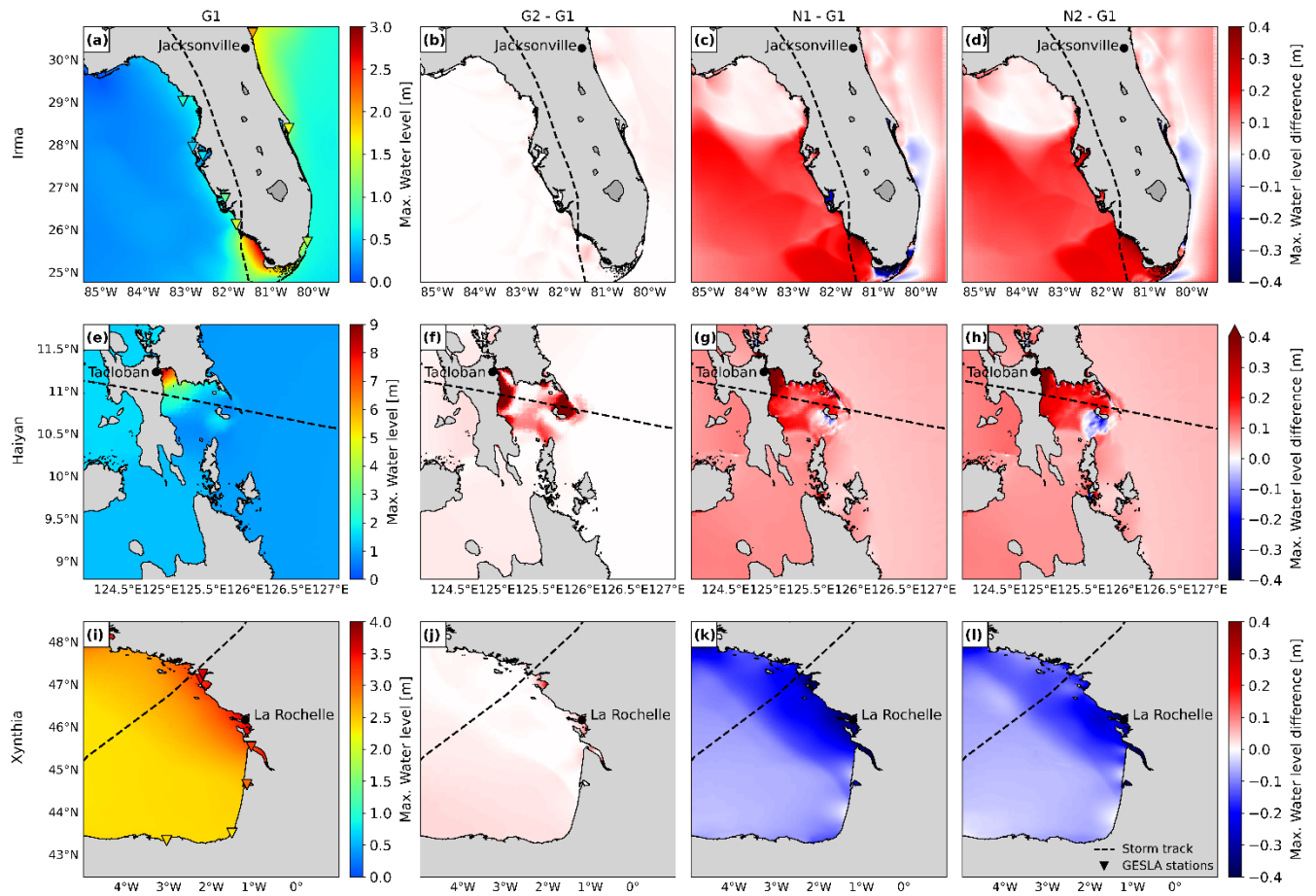


Figure 8. Maximum water levels for the three case studies for G1 (panels a, e, i). Difference between the maximum water level for each specific model configuration (see Table 1) and G1. Panels a, e, i show observed maximum water level from tide gauge stations of GESLA. Difference in water levels for G2 (panels b, f, j), N1 (panels c, g, k) and N2 (panels d, h, l).

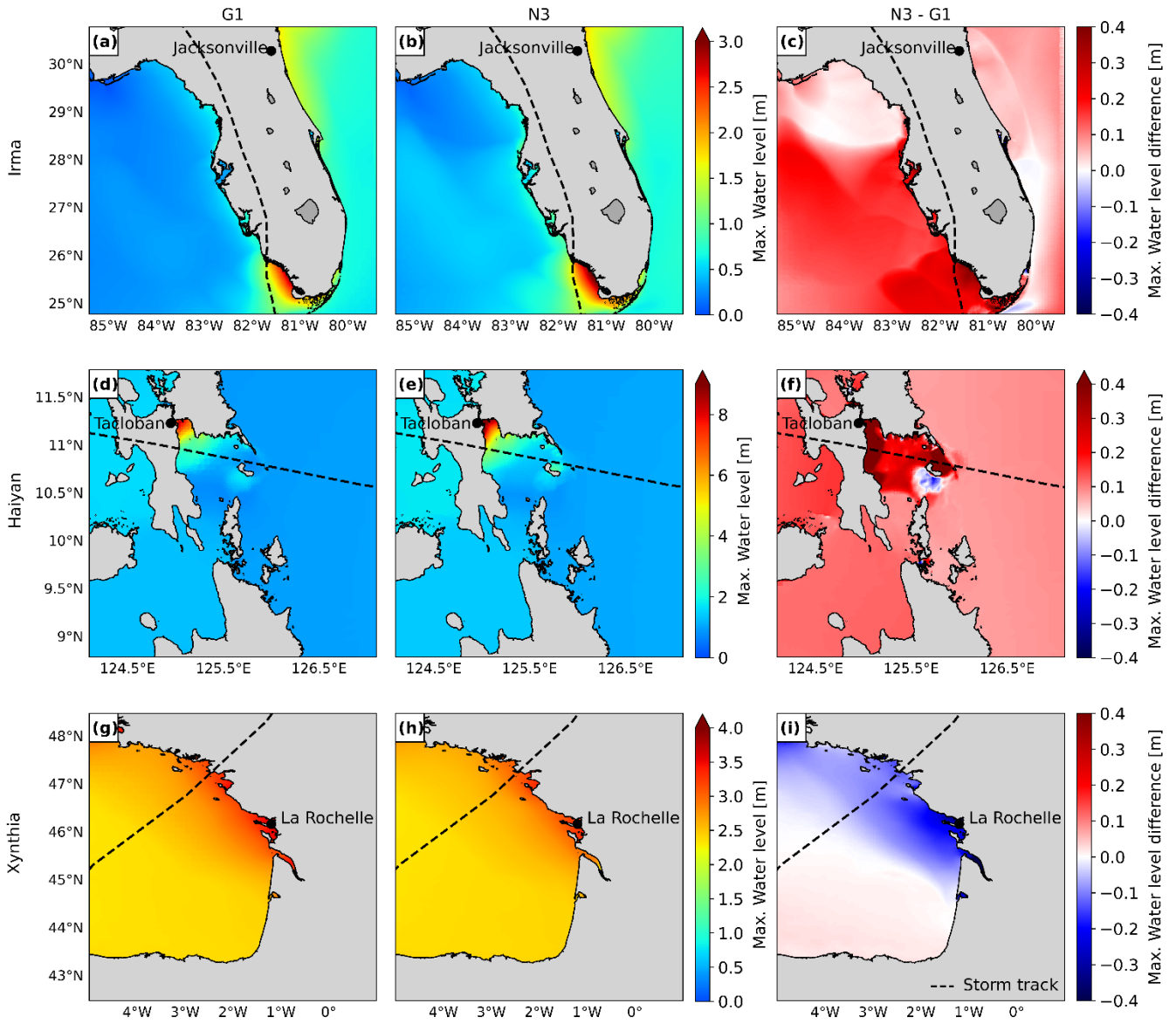
3.1.4 Effects of a fully refined model on total water levels

As a first step in the sensitivity analysis, we compare the maximum total water levels of the fully refined configuration and the default configuration. In Fig. 9 we observe that the maximum water level differences between the fully refined N3 and the default configurations G1 lead to significantly different results for each case study. For TC Irma the fully refined configuration N3 provides higher maximum water levels throughout almost the whole the domain, with maximum water levels up to 7.9 m, while the default configuration reaches 7.5 m resulting in a picture similar to N2 but with higher water levels along the southeast coast. The maximum differences in maximum water levels between N3 and N1 are up to approximately 0.5-3 m. For TC Haiyan the fully refined N3- provides maximum water levels that resemble a combination of G2 in the regions where temporal refinement is relevant, and N2 in the rest of the study area. The differences between N3 and G1 and default configurations provide maximum water levels up to 13.5 m. However, there are differences in maximum water levels for Haiyan are more than 24 m in the coast near Tacloban, both higher and lower than the default configuration depending on the region of the model domain. Finally, for ETC Xynthia the fully refined configuration N3 provides slightly higher maximum water levels in the south of the domain compared to G1, where the effects of G2 predominate, and lower lower maximum water

563

levels across the whole domain in the north, where the effects of N2 are more dominant, being up to 0.3 m lower than the default configuration.

564



565

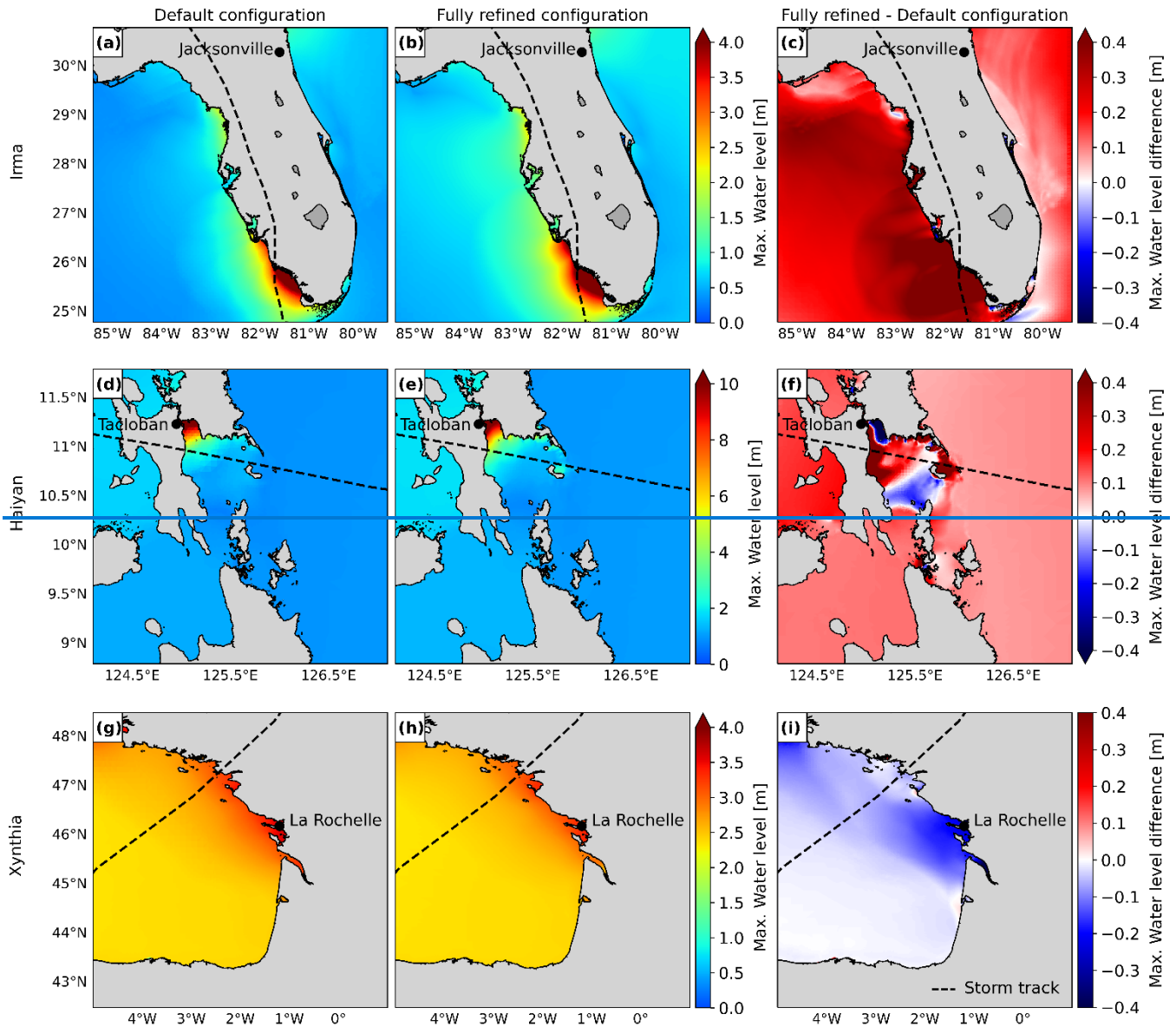


Figure 9. Maximum water levels for the three case studies, for the default configuration G1 (panels a, d, g) and for the fully refined configuration N3 (panels b, e, h). Difference between the maximum water level for N3 model configuration and G1 (panels c, f, i).

As a first step in the sensitivity analysis, we compare the maximum total water levels of the fully refined configuration and the default configuration. In Fig. 4 we observe that the maximum water level differences between the fully refined and the default configurations lead to significantly different results for each case study. For TC Irma the fully refined configuration provides higher maximum water levels throughout almost the whole the domain, with maximum water levels up to 7.9 m, while the default configuration reaches 7.5 m. The maximum differences in maximum water levels are up to approximately 0.5 m. For TC Haiyan the fully refined and default configurations provide maximum water levels up to 13.5 m. However, there are differences in maximum water levels for Haiyan of more than 1 m both higher and lower than the default configuration depending on the region of the model domain. Finally, for ETC Xynthia the fully refined configuration provides lower maximum water levels across the whole domain, being up to 0.3 m lower than the default configuration.

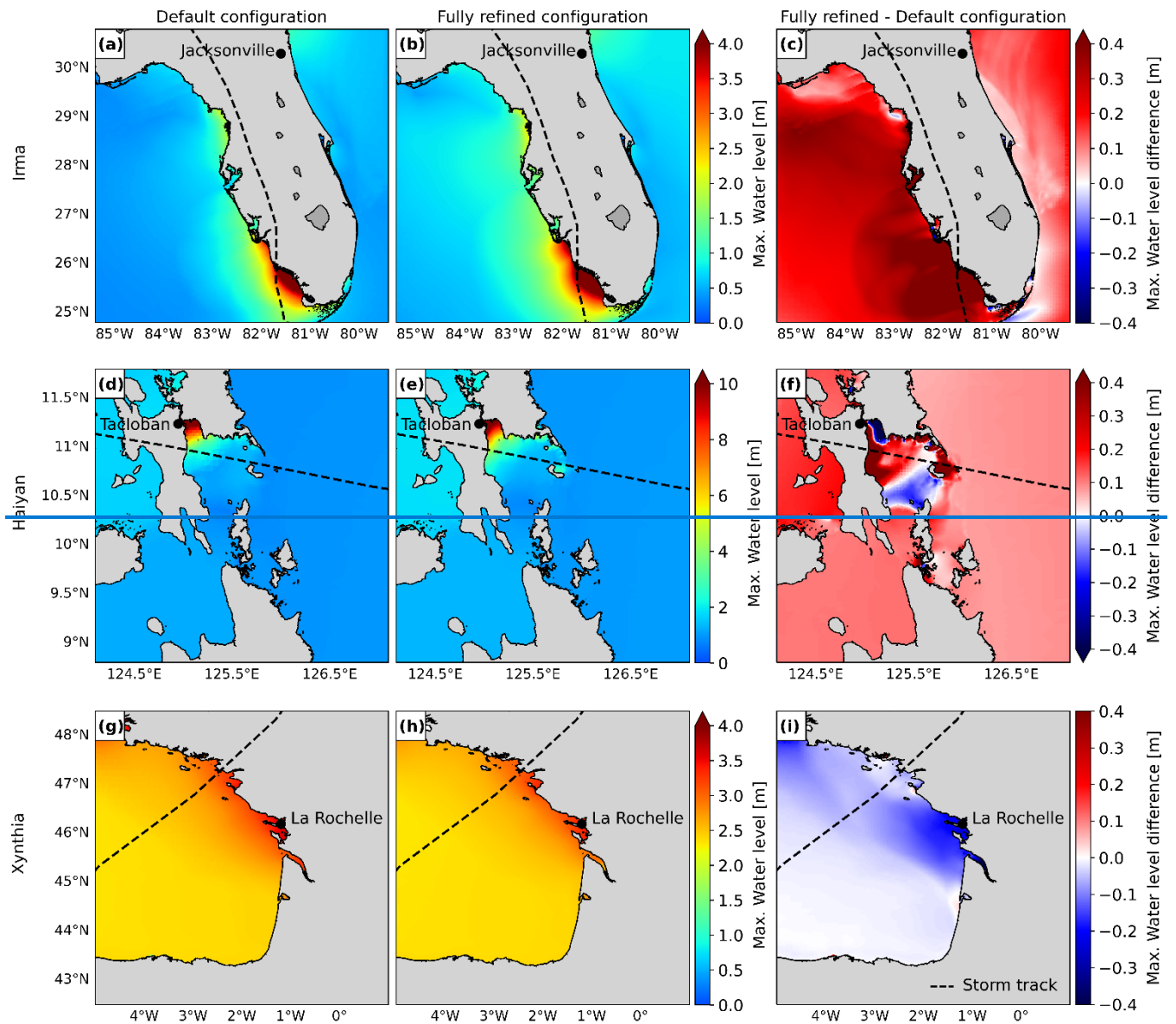


Figure 4. Maximum water levels for the three case studies, for the default configuration (panels a, d, g) and for the fully refined configuration (panels b, e, h). Difference between the maximum water level for the fully refined model configuration and the default configuration (panels c, f, i).

To understand the contribution of each refinement in the maximum water level differences between the fully refined configuration and the default configuration, Fig. 5 presents the differences in maximum water levels between each refinement and the default configuration. Refining the temporal output resolution of GTSM from 1-hourly to 10-minute intervals (Fig. 5 panels b, e, h) results in higher maximum water levels across the entire model domain for all three case studies. For TC Irma (Fig. 5 panel b), the sensitivity of the water levels to the temporal refinement is relatively small, up to 20 cm. Water levels increase due to the temporal output refinement mostly at the location of landfall, south of Florida, while near Jacksonville the water level changes are much smaller. The cause for this might be the fact that TC Irma did not directly pass over Jacksonville, therefore the storm surge generated in that region is mainly being driven by less intense outer winds that are less sensitive to changes in temporal resolution. For TC Haiyan (Fig. 5 panel e), the sensitivity of the water levels is significant. Water levels increase due to the temporal refinement up to about 1 m along the coastlines where TC Haiyan made landfall, showing that 1-hourly resolution is too coarse to accurately capture the water levels response. The cause for this might be that TC Haiyan had a rapid intensification, and when modelling water levels at 1-hourly resolution we might overlook the storm's peak, resulting in an underestimation of the maximum water levels. For ETC Xynthia (Fig. 5 panel h), the sensitivity of the water

596 *levels to the temporal refinement is relatively small, up to 10 cm. The small changes in water levels for ETC Xynthia are likely*
597 *due to the inherent characteristics of ETCs, which typically have larger dimensions, lower intensity, and a slower rate of*
598 *intensification compared to TCs. This means that the changes in meteorological forcing can be well captured at a 1-hourly*
599 *resolution.*

600 *Refining the spatial output resolution is not shown in Fig. 5 because increasing the number of water level locations does not*
601 *change the water level values themselves. However, this refinement becomes significant when these values are applied as*
602 *coastal boundary conditions to SFINCS (see Section 3.2), as a greater number of coastal boundary conditions offer additional*
603 *information for the flood model. (Haigh et al., 2023)*

604
605 *Dynamic downscaling (Fig. 5 panels c, f, i) results in relatively large changes in the water levels for all the case studies. The*
606 *largest differences occur along the coasts. For TC Irma (Fig. 5 panels c), the nesting of a local model at high resolution results*
607 *in maximum water levels that are about 0.5 m higher than the default configuration in the south of Florida. Those differences*
608 *might be due to changes in the bathymetric data from GEBCO2014 to GEBCO2023, which can resolve better the shallow*
609 *regions around the landfall location and due to the grid refinement of the region near landfall, which provides more accuracy*
610 *around the barrier islands, allowing to resolve better the water levels. Near Jacksonville, approximately 500 km distance from*
611 *the landfall location, the difference in maximum water levels instead are approximately 0.1 m higher. For TC Haiyan (Fig. 5*
612 *panels f), the differences in maximum water levels are approximately up to 0.4 m higher and lower than the default*
613 *configuration near the landfall regions. These differences might occur due to the update in bathymetry, where certain areas are*
614 *shallower and certain areas deeper for GEBCO2023 in comparison to the default GEBCO2014 dataset. Furthermore, the*
615 *refinement in the grid from 2.5 km to 45 m results in a significant increase in the number of model grid cells that define regions*
616 *of shallow bathymetry, especially around the bay near Tacloban, resulting in a more detailed resolution of water levels in that*
617 *region. Thanks to the increase on grid cells, on the strait north of Tacloban GTSM is able to better resolve the water levels,*
618 *and therefore, water can travel northwards. For ETC Xynthia (Fig. 5 panels i), the water levels from the nested local model at*
619 *high resolution are overall lower than water levels for the default configuration. Near La Rochelle, those water levels are*
620 *approximately 0.3 m lower. The reason for this might be due to differences in the bathymetry in the region around La Rochelle,*
621 *and due to the fact that the refined grid has more grid cells that resolve the water travelling through the estuaries in the region.*

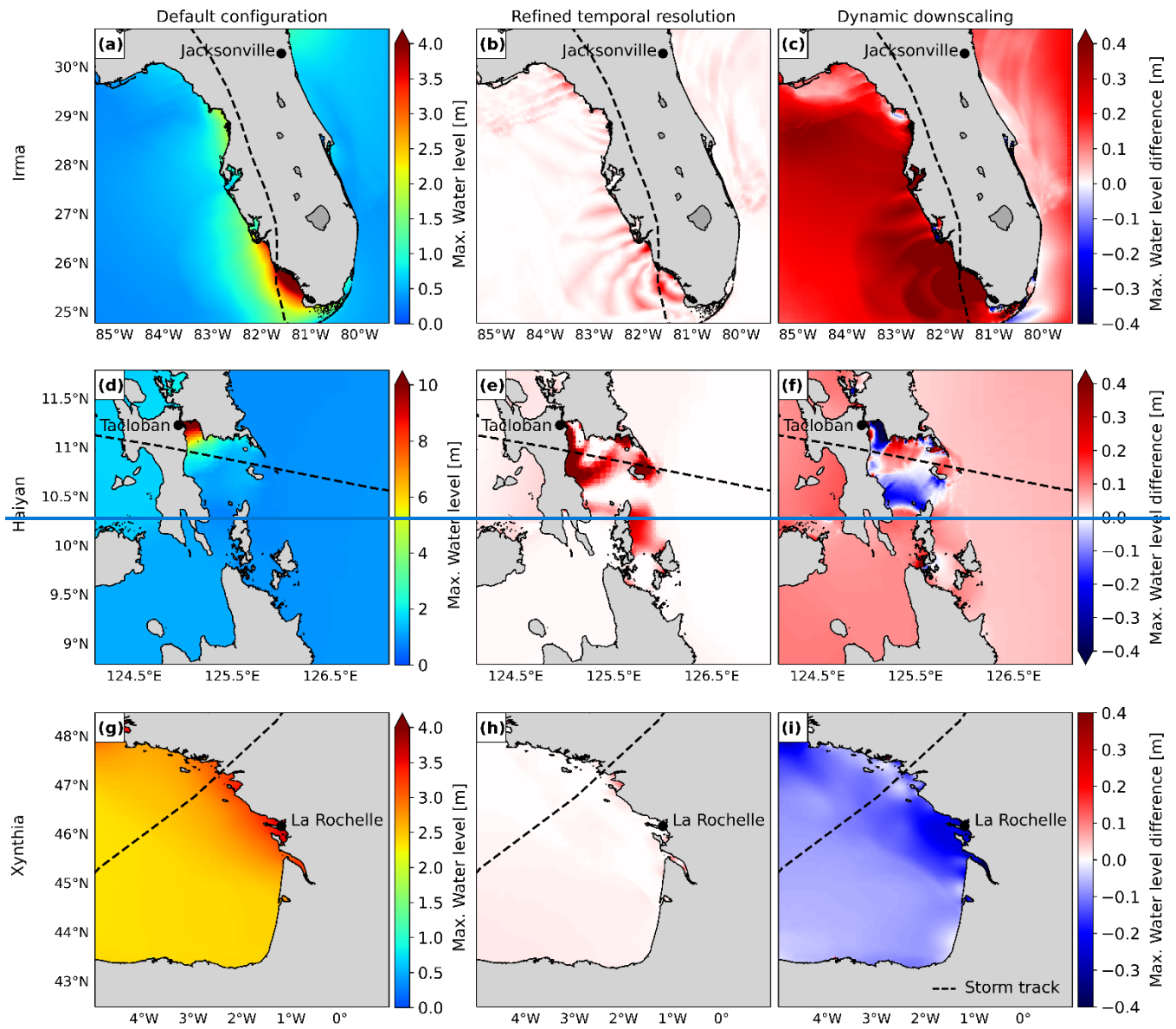


Figure 5. Maximum water levels for the three case studies, for the default configuration (panels a, d, g). Difference between the maximum water level for each specific model configuration and the default configuration. Difference in water levels for the temporal output resolution refined configuration (panels b, e, h) and the dynamic downscaling configuration (panels c, f, i).

3.2 Hydrodynamic flood modelling

As a second step in the sensitivity analysis, we analyse how the effects of the different storm surge model configurations propagate to the SFINCS flood model. compare the maximum flood depth of the fully refined configuration and the default configuration. In Figure 10 we compare the maximum flood depths of each refinement and G1. Figure 11 In Fig. 6 we observe that shows the maximum flood depth differences between the fully refined and the default configuration lead to different results for each case study N3 and G1.

3.2.1 Effects of higher resolution on flood depths

Figure 10 panels b, g, i show that To understand the contribution of each refinement in the maximum flood depth differences between the fully refined configuration and the default configuration. Fig. 7 presents the differences in maximum flood depths between each refinement and the default configuration.

the refinement of GTSM's temporal output resolution from 1-hourly to 10-minute intervals of G2 (Fig. 7 panels b, f, i) provides different results for each case study. For TC Irma (Fig. 107 panel b), the small increase in water levels as a result

693 of the temporal output refinement (Section 3.1.1-3.1.4) also results in a small increase in flood depths. Conversely, TC Haiyan
694 (Fig. 10 panel Fig. 7 panel f) experiences much higher water levels along the coast at higher temporal resolution. As a result,
695 it also experiences significantly higher flood depths, surpassing G1 the default configuration by 1 m in regions near Tacloban.
696 ETC Xynthia (Fig. 10 panel Fig. 7 panel j) experiences an increase in water levels along the coast for the 10-minute temporal
697 output resolution, especially in the study region of SFINCS. This which results in an increase in flood depths of up to 0.1 m.
698 For ETC Xynthia, G2 shows a higher hit rate and false-alarm ratio compared to G1, but the same critical success index (see
699 Fig. A9).

700 Figure 10 panels c, h, m show that refinement of Refining the spatial output locations from GTSM of G3 provides coastal
701 boundary conditions to SFINCS at additional locations, thereby improving the providing more accuracy of the water levels
702 input to the flood model. panel c shows that this refinement results in lower flood depths north of and around Jacksonville for
703 TC Irma. Conversely, for TC Haiyan (Fig. 10 7-panel h), the increase in spatial inputs results in higher flood depths in most
704 of the study area, particularly exceeding more than 1 m the default configuration G1 flood depths around Tacloban. For ETC
705 Xynthia (Fig. 10 7-panel k) the refinement of spatial water level inputs overall leads to higher flood depths, being north of
706 La Rochelle of up to 0.1 m-, while south of La Rochelle there are barely any changes compared to G1 higher. For ETC Xynthia,
707 G3 shows the same hit rate as G1, higher false-alarm ratio and the same critical success index (see Fig. A9).

708 3.2.2 Effects of dynamic downscaling with original bathymetry on flood depths

709 Figure 10 panels d, i, n show that the model configuration N1 results in significant changes in the flood depths for all the case
710 studies. For TC Irma (Fig. 10 panel d), model configuration N1 leads to slightly higher water levels in comparison to G1.
711 Consequently, the resulting flood depths are also larger and are more than 0.2 m above those of G1. Maximum water levels
712 for TC Haiyan (Fig. 10 panel i) are generally higher along the bay of Tacloban when applying dynamic downscaling with the
713 original bathymetry. This results on average in higher flood depths of more than 1 m compared to G1. Finally, ETC Xynthia
714 (Fig. 10 panel n) presents lower water levels for N1 compared to G1. Those lower water levels lead to lower flood depths
715 across the whole model domain. For ETC Xynthia, N1 shows a lower hit rate and false-alarm ratio compared to G1, and the
716 same critical success index (see Fig. A9).

717 3.2.3 Effects of dynamic downscaling with updated bathymetry on flood depths

718 Figure 10 panels e, j, o show that the model configuration N2 results in significant changes in flood depths for all case studies.
719 For TC Irma (Fig. 10 panel e), model configuration N2 compared to G1 leads to higher and lower water levels, depending on
720 the region. Consequently, the resulting flood depths for N2 vary between 0.05 m lower to more than 0.2 m higher than G1.
721 Maximum water levels for TC Haiyan (Fig. 10 panel Fig. 7 panel h) are generally higher in the bay of Tacloban for model
722 configuration N2 (when applying dynamic downscaling with the updated bathymetry) compared to G1 when applying dynamic
723 downscaling, resulting in lower flood depths. This results in larger flood depths which, in some regions, result in more than 1
724 m higher compared to G1. However, in the Tacloban Bay N1 results on average in higher maximum water levels than N2,
725 which leads to lower flood depths for N2 in comparison to N1 On the strait north of Tacloban, GTSM is able to better resolve
726 the water levels, and therefore, water can travel north, leading to higher flood depths along the strait. Finally, for ETC Xynthia
727 (Fig. 10 panel Fig. 7 panel o) water levels are lower for N2 compared to G1 has lower water levels due to the dynamic
728 downscaling. Those lower water levels lead to lower flood depths across the whole model domain. For ETC Xynthia, N2
729 shows a lower hit rate and false-alarm ratio compared to G1, and the same critical success index (see Fig. A9). Those lower
730 water levels lead to lower flood depths across the whole model domain.

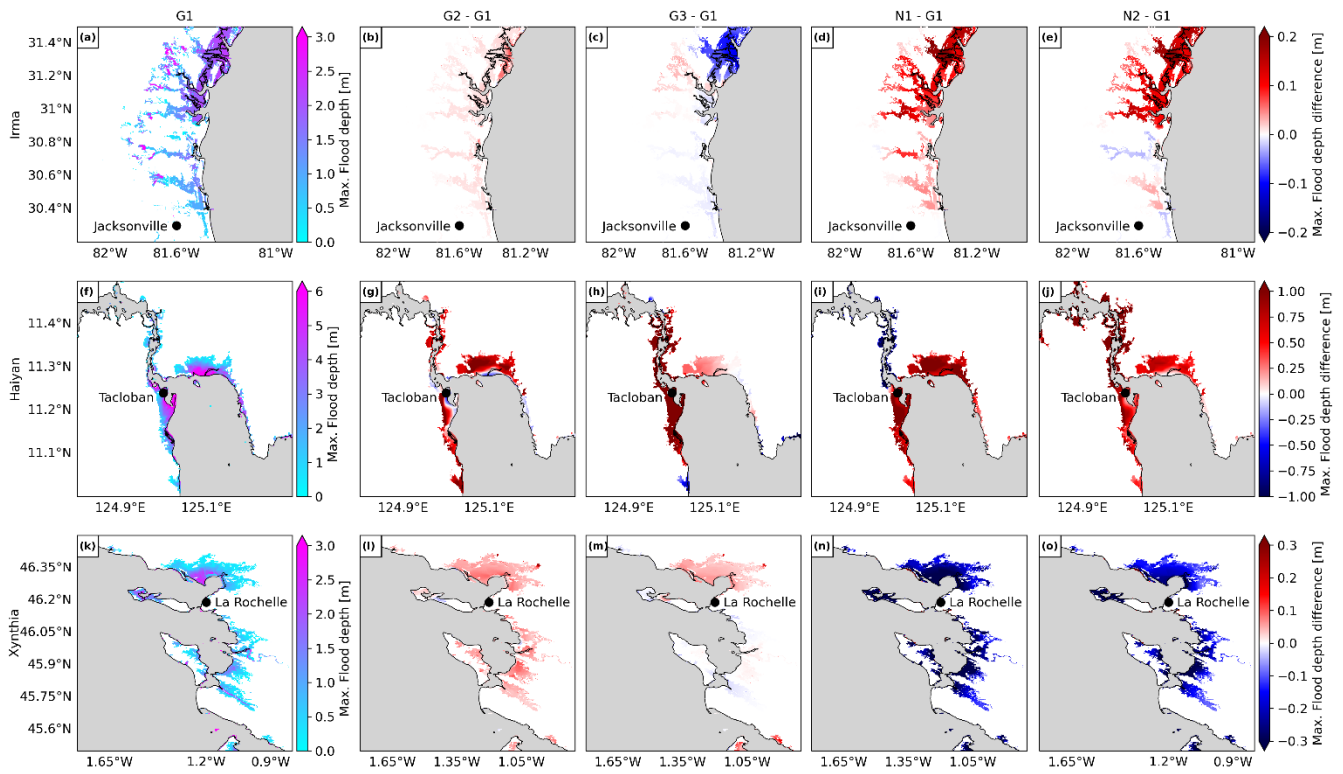
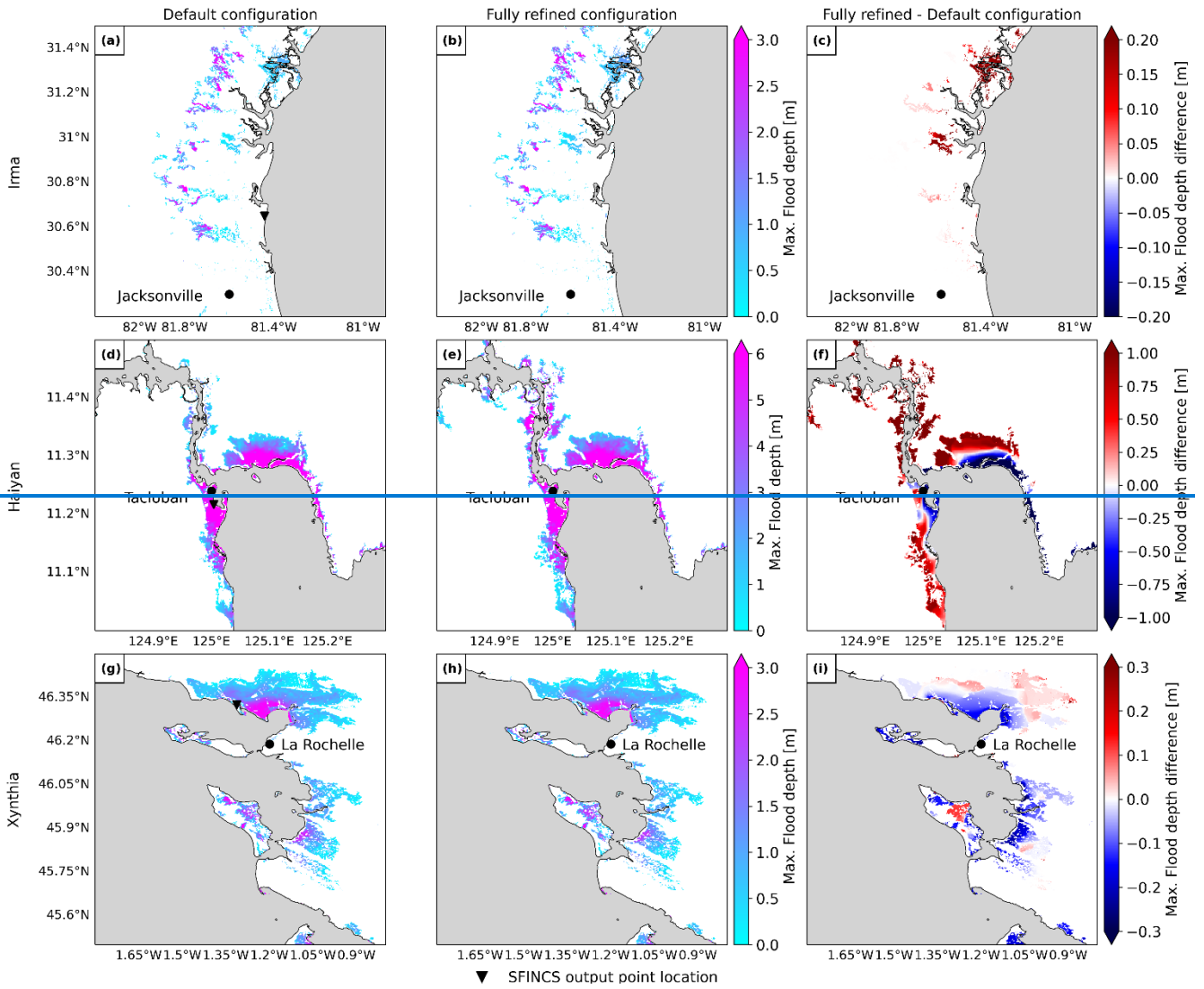
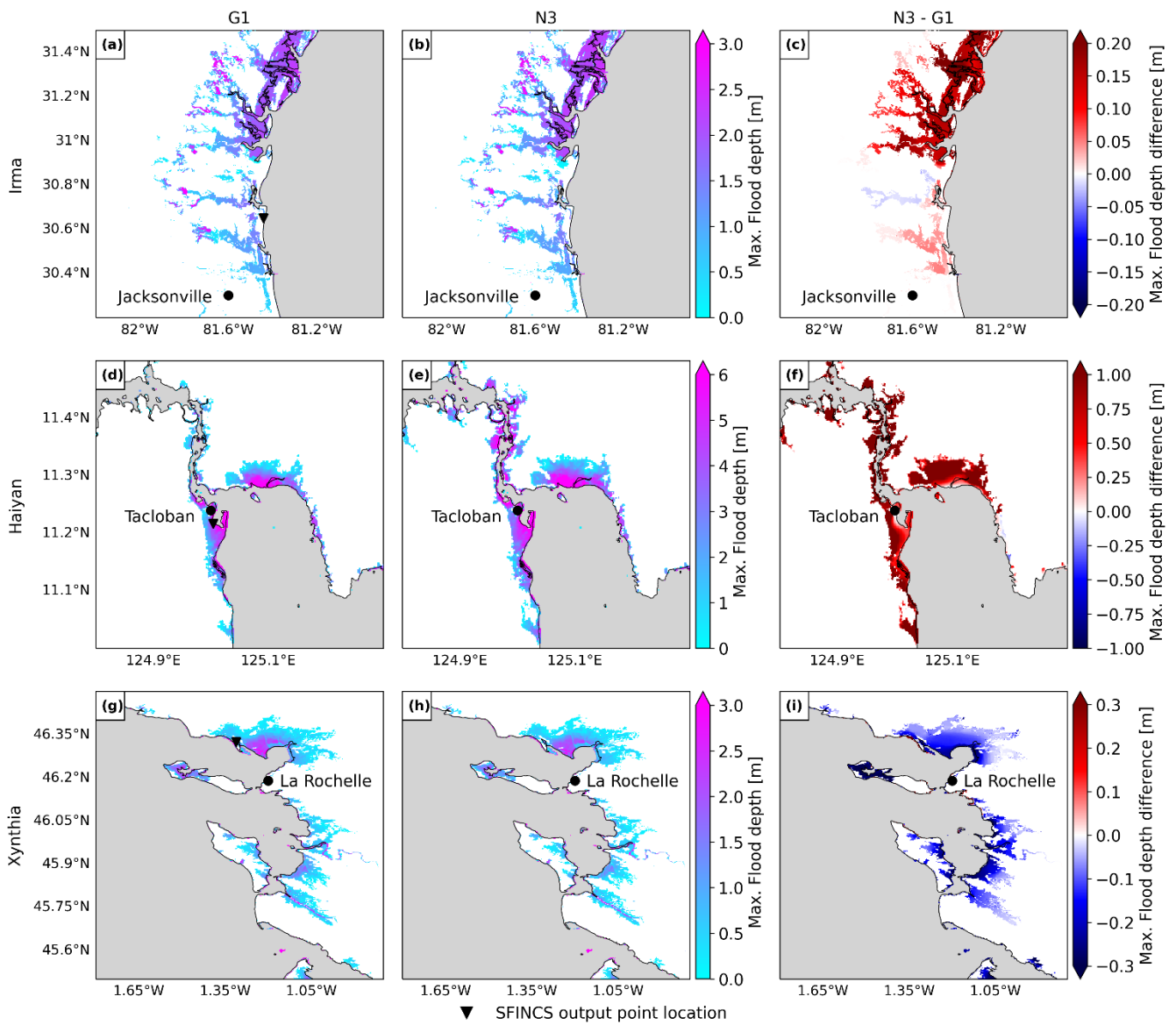


Figure 10. Panels a, f, k show the maximum flood depth for the default configuration G1, for each case study. Panels b, g, l show the difference between the maximum flood depth for the refined temporal output resolution configuration G2 and G1. Panels c, h, m show the difference between the maximum flood depth for the refined spatial output configuration G3 and G1. Panels d, i, n show the difference between the maximum flood depth for the dynamic downscaling (refined grid) configuration N1 and G1. Panels e, j, o show the difference between the maximum flood depth for the dynamic downscaling (refined grid and updated bathymetry) configuration N2 and G1.

3.1.13.2.4 Effects of a fully refined model on flood depths

As a second step in the sensitivity analysis, we compare the maximum flood depth of the fully refined configuration and the default configuration. In Fig. 6 we observe that the maximum flood depth differences between the fully refined and the default configuration lead to different results for each case study. For TC Irma the fully refined configuration N3 provides higher water levels throughout large parts of the whole domain (Section 3.1.4.3.4) that translate into higher flood depths up to more than 0.2 m near Jacksonville. For TC Haiyan, on the one hand the fully refined configuration N3 provides lower-high water levels near Tacloban (Section 3.1.4.3.1), translating into lower-high flood depths, up to more than 1 m while on the other hand, regions south of Tacloban and north of the bay experience higher water levels that translate into higher flood depths as compared to the default configuration. Finally, ETC Xynthia presents lower water levels for for the fully refined configuration N3 near La Rochelle (Section 3.1.4.3.1), which that translate into lower flood depths along the coast, up to approximately 0.3 m across the whole domain. Further inland, however, flood depths are higher than for the default configuration.





752

753 **Figure 116.** Panels a, d, g show the maximum flood depth for the default configuration **G1** for each case study. Panels b, e, h show
 754 the maximum flood depth for the fully refined configuration **N3**. Panels c, f, i show the difference between the maximum flood
 755 depth for **the fully refined N3** and **the default configuration G1**.

756

To understand the contribution of each refinement in the maximum flood depth differences between the fully refined configuration and the default configuration, Fig. 7 presents the differences in maximum flood depths between each refinement and the default configuration.

759

Refining GTSM's temporal output resolution from 1 hourly to 10 minute intervals (Fig. 7 panels b, f, j) provides different results for each case study. For TC Irma (Fig. 7 panel b), the small increase in water levels as a result of the temporal output refinement (Section 3.1) also results in a small increase in flood depths. Conversely, TC Haiyan (Fig. 7 panel f) experiences much higher water levels at higher temporal resolution. As a result, it also experiences significantly higher flood depths, surpassing the default configuration by 1m in regions near Tacloban. ETC Xynthia (Fig. 7 panel j) experiences an increase in water levels along the coast for the 10 minute temporal output resolution, which results in a general increase in flood depths of approximately 0.1 m.

766

Refining the spatial output locations from GTSM provides coastal boundary conditions to SFINCS at additional locations, thereby improving the accuracy of the water levels input to the flood model. Figure 7 panel c shows that this refinement results

767

in lower flood depths north of Jacksonville for TC Irma. Conversely, for TC Haiyan (Fig. 7 panel g), the increase in spatial inputs results in higher flood depths in most of the study area, particularly exceeding 1 m the default configuration flood depths around Tacloban. For ETC Xynthia (Fig. 7 panel k) the refinement of spatial water level inputs overall leads to higher flood depths, being north of La Rochelle approximately 0.1 m higher.

Dynamic downscaling for TC Irma (Fig. 7 panel d) leads to higher water levels in comparison to the default configuration. Consequently, the resulting flood depths are also higher, exceeding approximately 0.2 m above those of the default configuration. Model results for TC Haiyan (Fig. 7 panel h) generally result in lower water levels in the bay of Tacloban when applying dynamic downscaling, resulting in lower flood depths. On the strait north of Tacloban, GTSM is able to better resolve the water levels, and therefore, water can travel north, leading to higher flood depths along the strait. Finally, ETC Xynthia (Fig. 7 panel l) has lower water levels due to the dynamic downscaling. Those lower water levels lead to lower flood depths across the whole model domain.

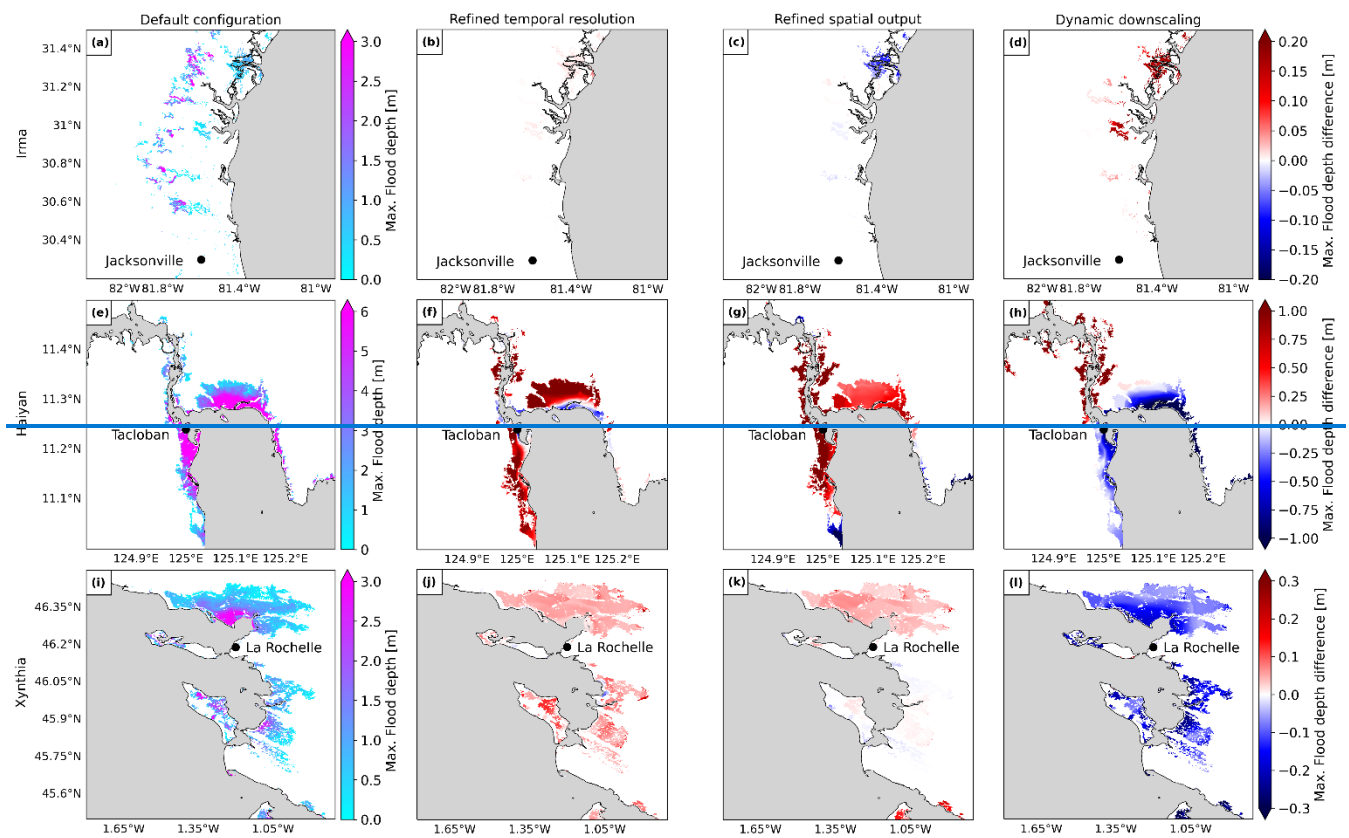


Figure 7. Panels a, e, i show the maximum flood depth for the default configuration for each case study. Panels b, f, j show the difference between the maximum flood depth for the temporal refined configuration and the default configuration. Panels c, g, k show the difference between the maximum flood depth for the refined spatial output configuration and the default configuration. Panels d, h, l show the difference between the maximum flood depth for the dynamic downscaling configuration and the default configuration.

To analyse the changes of flood depths over time, Fig. 128 panels a, b, c show the flood depth timeseries at the SFINCS output point locations outlined in Fig. 116, for the default all the model configurations and fully refined configurations as well as the three individual refinements. While the timing and shape of the flood depth timeseries remains consistent across all the model configurations for all the case studies, an only slight there are differences in the magnitude of the flood depths are visible. Figure 128 panel a shows that for TC Irma the fully refined configuration leads to higher flood depths than those for the default configuration. It can be observed that the cause for that increase in flood depths is mostly triggered by the dynamic

858 downscaling, which results in flood depths more than 0.5 m higher than those with the default configuration, all the model
859 configurations result in similar flood depths, and only N1 results in slightly higher flood depths of about 0.1 m more than the
860 others. On the contrary, the temporal and spatial output refinements do not have much influence on the flood depths at this
861 SFINCS output point location. Figure 128 panel b shows that for TC Haiyan the fully refined configuration leads to similar
862 flood depths than those for the default configuration. G1 results in the lowest flood peak, while the temporal resolution of G2
863 plays a key role, enhancing the flood peak up approximately 1 m higher than G1. It can be observed that refining the temporal
864 and spatial output resolution results in flood depths approximately 1 m higher than the default configuration. However, the
865 dynamic downscaling produces lower flood depths, compensating the other refinements and leading to similar results for the
866 fully refined and default configurations at the peak of the event. A smaller flood peak occurs around 05:00 on the 8th of
867 November, where the timing of the fully refined configuration occurs earlier, probably as an effect of the temporal output
868 resolution refinement. Finally, Fig. 128 panel c shows that for all global model configurations (G1, G2 and G3) result in a first
869 flood peak that is approximately 0.5 m higher than those of the nested model configurations (N1, N2 and N3). The second
870 peak is simulated more similarly by all model configurations, being N1 the configuration that provides lowest flood depths.
871 ETC Xynthia the fully refined configuration leads to lower flood depths than those for the default configuration. The results
872 of the fully refined configuration seem mostly influenced by the dynamic downscaling but with higher flood depths at the
873 flood peaks of the event, which could be the result of the temporal and spatial output refinements.

874 Panels a, b, c in Fig. 128 only show the results for a single SFINCS output point location. However, the refinements that has
875 the most effect on the fully refined configuration might have most effect in other regions different might be different when
876 looking at other than the SFINCS output point locations. For TC Haiyan, for example, when looking at Fig. 6 and Fig. 7 we
877 observe that the water levels and resulting flood depths for the fully refined configuration are similar to those for the dynamic
878 downscaling near Tacloban, while south of Tacloban the temporal and spatial output refinements seem to be more dominant.
879 For ETC Xynthia, when looking at Fig. 6 and Fig. 7 we observe that the flood depths for the fully refined configuration are
880 similar to those for the dynamic downscaling along the coasts, but further inland the temporal and spatial output refinements
881 seem more dominant. To understand the overall effect of each refinement in the flood hazard maps in the fully refined
882 configuration, Fig. 128 panels d, e, f show the flood volume timeseries across each of the case study's model domain. While
883 the timing and shape of the flood volume timeseries remains consistent across all the model configurations for all the case
884 studies, there are differences in the magnitude of the flood volumes. Figure 128 panel d shows that for TC Irma the
885 nested models the fully refined configuration leads to the highest flood volumes than those for the default configuration, being
886 N3 the model configuration that simulates the highest flood volume. On the other hand, the increase in spatial output of GTSM
887 from G3 results in the lowest flood volumes. It can be observed that the cause for that increase in flood volume is mostly
888 triggered by the dynamic downscaling, which results in flood volumes of more than $2 \times 10^7 \text{ m}^3$ than those with the default
889 configuration. On the contrary, the temporal output refinement does not have much influence on the flood volume, and the
890 spatial output refinement leads to lower flood volumes than the default scenario. Figure 128 panel e shows that
891 for TC Haiyan the fully refined configuration N3 also leads to the highest flood volumes, while G1 results in the lowest
892 volumes, leads to significantly higher flood volumes than those for the default configuration. At the peak of the event, the fully
893 refined configuration leads to approximately $2 \times 10^8 \text{ m}^3$ more than the default. This increase in volume seems to be the result
894 of a combination of all the refinements, with the increase in temporal output resolution being the refinement that leads to most
895 similar results. Finally, Fig. 128 panel f shows that for ETC Xynthia the fully refined configuration the nested model
896 configurations lead to the lowest flood volumes, while the global models result in higher flood volumes, presents similar flood
897 volumes as the default configuration. At the first flood peak, the flood volume provides similar results as the default, due to
898 the lower flood volumes caused by the dynamic downscaling that seem to compensate the higher volumes caused by the
899 temporal and spatial output refinements. In the second flood peak, however, the fully refined configuration shows lower flood

depths than those for the default configuration. The reason for this could be the fact that compared to the first peak, the dynamic downscaling in this peak presents lower flood volumes with respect to the default configuration.

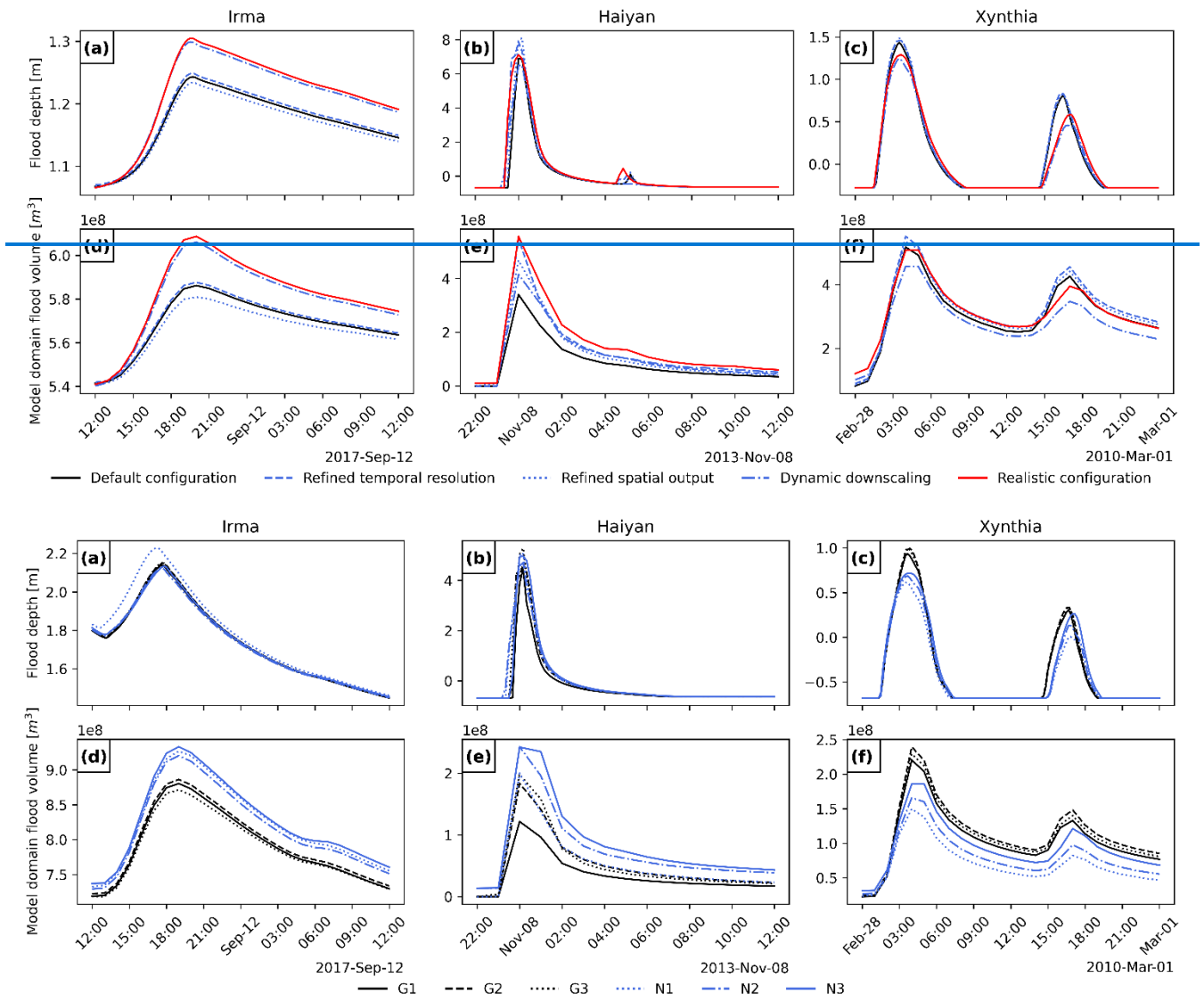


Figure 128. Flood depth timeseries for three observation points and flood volume timeseries for the SFINCS model domain of each case study and model configuration (see Table 1). The spatial location of the SFINCS output point locations can be observed in Fig. Figure 11 panels a, d, g6.

4 Discussion and Conclusions

The MOSAIC modelling framework introduced in this study allows to dynamically simulate coastal flooding events through MOSAIC enables the coupling of dynamic water level and overland flood models, making use of a Python environment. As such, this approach is automated and reproducible, and combined with the hydrodynamic models used, this makes the approach makes it globally applicable. MOSAIC's flexibility allows us to easily simulate coastal flooding events globally, while also allowing using for local high-resolution models, and its multiscale modelling approach also allows us to enhance the simulation at local scale by providing refined water levels. As such, MOSAIC provides a bridge between fully global and fully local modelling approaches, and thereby paves the way for more actionable large-scale flood risk assessments.

959 The results of the sensitivity analysis conducted in this study reveal the complexity of hydrodynamic modelling and the
960 sensitivity to specific local settings and storm characteristics. A comparison of the fully refined N3 configuration with the
961 default G1 configuration reveals differing behaviours across the case studies in terms of changes in water levels and flood
962 depths, both spatially and in magnitude. When comparing the fully refined and the default configurations, the behaviour of
963 each case study differs in terms of changes in water levels and flood depth, both, spatially and in magnitude. For instance,
964 model configuration N3 simulates higher water levels almost everywhere for TC Irma. However, for TC Haiyan and ETC
965 Xynthia, certain regions show higher water levels with N3, while others show lower water levels compared to G1. Similarly,
966 flood depths around Jacksonville for TC Irma are generally higher with N3, although some areas experience lower values. In
967 contrast, for TC Haiyan in Tacloban, flooding significantly increases with N3, whereas for ETC Xynthia flood depths decrease
968 notably around La Rochelle. ~~the fully refined configuration~~

969 ~~Refining the temporal output resolution results in higher water levels and flood depths, while for TC Haiyan it results in region~~
970 ~~with higher and regions with lower water levels and flood depths, and for ETC Xynthia water levels become lower overall,~~
971 ~~and flood depths result lower along the coast but higher further inland.~~ ~~The effects of refining the temporal output~~
972 ~~resolution (model configuration G2) on the one hand seem to have large~~ has a significant influence for on small, rapidly
973 intensifying TCs like Haiyan, resulting in water levels and flood depths that are 2 m and 1 m, ~~resulting in water levels and~~
974 ~~flood depths more than 0.5 m and 1 m higher~~ higher, respectively, compared to G1 for TC Haiyan, respectively. On the other
975 ~~hand~~ However, for ETCs, the ~~refining-refinement of the~~ temporal output resolution does ~~not not change~~ lead to substantial
976 changes in the water levels ~~and or~~ flood depths ~~significantly, being with a~~ 1-hourly temporal resolution ~~enough~~ providing
977 sufficiently accurate results. Refining the spatial output locations of GTSM (model configuration G3) provides more coastal
978 boundary conditions for SFINCS, ~~resulting always in more accurate flood depth results.~~ ~~However, f~~ For regions where the
979 water levels have more spatial heterogeneity along the coast, this refinement becomes most relevant. For TC Haiyan, for
980 example, the coastal boundary conditions in the bay of Tacloban raised from 4 locations to more than 20 (see Fig. 7), this
981 refinement lead ings to flood depths 1 m higher than ~~the default configuration~~ G1. Furthermore, regions with more complex
982 topographies such as the south of Florida for TC Irma or the Tacloban bay for TC Haiyan are influenced by the grid refinement
983 of N1, leading to larger differences with G1 in terms of water levels and consequently, flooding. The choice of bathymetric
984 datasets also plays a role in the prediction of water levels, contributing to the differences observed between N1 and N2 in all
985 the case studies. ~~Furthermore, changes in water levels due to dynamic downscaling are notably affected by the bathymetry~~
986 ~~used to generate the local high-resolution models. This refinement leads to maximum water levels more than 0.5 m higher for~~
987 ~~TC Irma and 0.3 m lower for ETC Xynthia, in comparison to the default configuration. Looking at the effects of each~~
988 ~~refinement, we observe that while for TC Irma the refinement that most affects the model results is the dynamic downscaling,~~
989 ~~for TC Haiyan and ETC Xynthia the fully refined configuration seems to be a combination of all the refinements.~~ Based on
990 these results, we can conclude that the refinement of the global modelling approach can significantly impact the simulation of
991 coastal water levels and flood depths at local scale, although the differences in local settings make that there is no one-size-
992 fits-all approach and refinement does not per se lead to the best performing model.

993 The validation of the model configurations for the different case studies also highlights the complexities involved in refining
994 hydrodynamic models, and how each specific setting impacts overall performance. It is challenging to assess the performance
995 of global models due to the limited number of tide gauge stations available, meaning the validation results might not be fully
996 representative over the entire domain. Another source of uncertainty is the location of these tide gauge stations, which are
997 often situated in enclosed basins or harbours, where hydrodynamic models have more difficulty simulating water levels
998 compared to open sea conditions. While the performance indicators from this study, with Pearson's correlations above 0.92
999 and RMSEs in general less than 0.3 m, suggest that all the refinements perform adequately and similarly to G1, the validation
1000 does not allow us to determine which model configuration consistently provides the best overall performance. This outcome

1001 largely depends on the storm characteristics and regional topography. However, the flexibility and ease of use of MOSAIC, as
1002 a Python-based framework, make it a valuable resource for users to further explore which are the optimal settings for their
1003 case study and region of interest.

1004 ~~we conclude that refinement of the global modelling approach can significantly impact the simulation of coastal water levels~~
1005 ~~and flood depths at local scale. This highlights the potential merit of a multiscale modelling approach within local refinement~~
1006 ~~as applied in MOSAIC.~~

1007 There are several limitations that need to be taken into account when using MOSAIC. Limitations that are linked to general
1008 flood hazard modelling and not specific to MOSAIC include the following: (1) the meteorological forcing data can be a big
1009 source of uncertainty when modelling extreme water levels. MOSAIC allows to combine the results of the Holland model with
1010 climate reanalysis datasets in the background to enhance the wind and pressure fields at the peripheries of the TCs. Nonetheless,
1011 the implementation of more advanced wind parametric models could further improve the water level simulations (Emanuel
1012 and Rotunno, 2011; Hu et al., 2011). (2) the accuracy of the bathymetry has a large influence on storm surge modelling
1013 (Bloemendaal et al., 2019; Dullaart et al., 2020; Mori et al., 2014). When performing dynamic downscaling, MOSAIC uses
1014 bathymetry data to generate the model grid and subsequently simulate total water levels. Using higher-resolution local
1015 bathymetry enables finer grid refinement and ~~enhances~~ can enhance the accuracy of the results. However, such high-resolution
1016 bathymetry is not always available. MOSAIC is set up to allow the substitution of bathymetric data with alternative datasets,
1017 to adjust the grid resolution and refinement, and to define the desired domain of the local high-resolution model. (3) digital
1018 elevation models (DEMs) can have a large influence on flood model simulations, affecting the flood hazard depth map results.
1019 In this paper we use the FABDEM's and IGN's datasets dataset, but MOSAIC allows to replace the DEM with ~~any higher~~
1020 ~~resolution local datasets dataset, when available. In addition to the effects of DEMs, the presence of flood protection structures~~
1021 ~~has substantial impact on flood hazard models. The neglect of dikes in our SFINCS model is one of the reasons our~~
1022 ~~modelling framework overestimates flooding for ETC Xynthia. MOSAIC's HydroMT component allows for the integration~~
1023 ~~of flood protection measures supports the implementation of levees as 1D line features into the SFINCS model, and this~~
1024 ~~capability could be used within MOSAIC upon the availability of flood protection data.~~

1025 MOSAIC's main limitation lies in the generation of the local high-resolution models for dynamic downscaling. These
1026 automatically generated local high-resolution models can present instabilities when refined grid cells are present at the model
1027 boundaries. Therefore, care needs to be taken when applying dynamic downscaling. To solve this problem the first 0.3 degrees
1028 around the model domain are not being refined in this study. When changes in grid refinement are abrupt, model instabilities
1029 can also occur. The nesting of multiple models in each other would allow for a smoother grid transition and might solve this
1030 issue.

1031 In this study, we have implemented MOSAIC to simulate ~~TC and ETC~~ coastal flooding ~~driven by as a result of~~ storm surges.
1032 ~~However, since flooding typically results from a combination of various drivers, our results currently underestimate flooding~~
1033 ~~near estuaries and deltas due to the exclusion of precipitation and river discharge, and near steep coasts due to the exclusion~~
1034 ~~of waves and overtopping.~~ Future research on TCs and ETCs may further develop MOSAIC and include other drivers such as
1035 waves, rainfall and discharge. Considering that HydroMT and SFINCS are capable of handling compound flooding induced
1036 by pluvial and fluvial drivers (Eilander et al., 2023), there is potential for future enhancements of MOSAIC to incorporate the
1037 modelling of compound events. Furthermore, MOSAIC currently makes use of offline coupling for both the local-high
1038 resolution model and the SFINCS model. However, new software developments such as ~~the~~ Oceanographic Multi-purpose
1039 Software Environment (OMUSE; Pelupessy et al., 2017) could be used in the future to move from offline to online coupling,
1040 and to further expand MOSAIC by allowing for coupling with other models such as hydrological or ocean models.

1041 ~~The flexibility of MOSAIC to modify the input datasets could be leveraged to study events under historical and climate change~~
1042 ~~conditions. Furthermore, taking advantage of MOSAIC's multiscale modelling approach, TC/ETC high-resolution hazard~~
1043 ~~assessments can be obtained globally. When linked to impact models, MOSAIC could also be used for risk assessments.~~ Users
1044 of MOSAIC can easily simulate storm events in any region with this the modelling framework. First, they can select the
1045 appropriate meteorological forcing. Within MOSAIC, users can choose gridded meteorological data from reanalysis datasets
1046 or climate models to simulate ETCs or TCs, provided that the data accurately captures the TC wind and pressure fields (as
1047 seen with ETC Xynthia and TC Irma in this study). Alternatively, they can select a hybrid approach that combines the Holland
1048 model with ERA5 in the background when modelling smaller TCs with rapid intensification (such as TC Haiyan in this study).
1049 Depending on the specific storm simulated and study area, users can select different model refinements. For instance, the G2
1050 model configuration with refined temporal output resolution is suitable for rapidly intensifying storms, while nested models
1051 can help resolving the topography and bathymetry in regions with complex coastlines. If the users have coastal boundary
1052 conditions available, MOSAIC can automatically generate stand-alone local high-resolution Delft3D FM models (N1, N2,
1053 and N3 model configurations) without having to couple them with GTSM. Although uncalibrated, these model configurations
1054 demonstrate similar performance than the well-established global model GTSM (G1; see Section 3), but at a significantly
1055 lower computational cost. The hydrodynamic flood modelling part of MOSAIC offers user-defined settings as well, enabling
1056 users to, for instance, choose the most suitable DEM for their study area or implement flood protection measures through
1057 MOSAIC's HydroMT component.

1058 By leveraging ~~the flexibility of MOSAIC to modify the input datasets,~~ the modelling framework can be used ~~could be~~
1059 ~~leveraged to study events under historical- and climate change conditions. Furthermore, taking advantage of MOSAIC's~~
1060 ~~multiscale modelling approach, TC/ETC high-resolution hazard assessments can be obtained globally. When linked to impact~~
1061 ~~models, MOSAIC could~~ can also be used for risk assessments.

1063 **Data availability**

1064 The datasets compiled and/or analysed during the current study are available on Zenodo. *Note: to be published with Doi*
1065 *upon acceptance of the paper.*

1066 **Code availability**

1067 The underlying code for this study is available on [Zenodo](https://github.com/Ireneben73/mosaic_framework). *Note: to be published with Doi upon acceptance of the paper at*
1068 https://github.com/Ireneben73/mosaic_framework (last access: 11 October 2024).

1069 **References**

- 1070 Andersen, O.B., Knudsen, P., 2009. DNSC08 mean sea surface and mean dynamic topography models. J. Geophys. Res.
1071 Oceans 114. <https://doi.org/10.1029/2008JC005179>
- 1072 Bates, P.D., Horritt, M.S., Fewtrell, T.J., 2010. A simple inertial formulation of the shallow water equations for efficient
1073 two-dimensional flood inundation modelling. J. Hydrol. 387, 33–45. <https://doi.org/10.1016/j.jhydrol.2010.03.027>
- 1074 Bates, P.D., Quinn, N., Sampson, C., Smith, A., Wing, O., Sosa, J., Savage, J., Olcese, G., Neal, J., Schumann, G.,
1075 Giustarini, L., Coxon, G., Porter, J.R., Amodeo, M.F., Chu, Z., Lewis-Gruss, S., Freeman, N.B., Houser, T.,
1076 Delgado, M., Hamidi, A., Bolliger, I., E. McCusker, K., Emanuel, K., Ferreira, C.M., Khalid, A., Haigh, I.D.,
1077 Couasnon, A., E. Kopp, R., Hsiang, S., Krajewski, W.F., 2021. Combined Modeling of US Fluvial, Pluvial, and
1078 Coastal Flood Hazard Under Current and Future Climates. Water Resour. Res. 57, e2020WR028673.
1079 <https://doi.org/10.1029/2020WR028673>

1080 Batts, M.L., Cordes, M., Russell, L., Shaver, J., Simiu, E., 1980. Hurricane Wind Speeds in the United States. Natl. Bur.
1081 Stand. Build. Sci. Ser. 106. <https://doi.org/10.1061/JSDEAG.0005541>

1082 Bertin, X., Bruneau, N., Breilh, J.F., Fortunato, A.B., Karpytchev, M., 2012. Importance of wave age and resonance in storm
1083 surges: The case Xynthia, Bay of Biscay. *Ocean Model.* 42, 16–30. <https://doi.org/10.1016/j.ocemod.2011.11.001>

1084 Bloemendaal, N., Muis, S., Haarsma, R.J., Verlaan, M., Irazoqui Apecechea, M., de Moel, H., Ward, P.J., Aerts, J.C.J.H.,
1085 2019. Global modeling of tropical cyclone storm surges using high-resolution forecasts. *Clim. Dyn.* 52, 5031–5044.
1086 <https://doi.org/10.1007/s00382-018-4430-x>

1087 Breilh, J.F., Chaumillon, E., Bertin, X., Gravelle, M., 2013. Assessment of static flood modeling techniques: application to
1088 contrasting marshes flooded during Xynthia (western France). *Nat. Hazards Earth Syst. Sci.* 13, 1595–1612.
1089 <https://doi.org/10.5194/nhess-13-1595-2013>

1090 Buchhorn, M., Smets, B., Bertels, L., Roo, B.D., Lesiv, M., Tsendbazar, N.-E., Herold, M., Fritz, S., 2020. Copernicus
1091 Global Land Service: Land Cover 100m: collection 3: epoch 2018: Globe.
1092 <https://doi.org/10.5281/ZENODO.3518038>

1093 Bunya, S., Dietrich, J.C., Westerink, J.J., Ebersole, B.A., Smith, J.M., Atkinson, J.H., Jensen, R., Resio, D.T., Luettich, R.A.,
1094 Dawson, C., Cardone, V.J., Cox, A.T., Powell, M.D., Westerink, H.J., Roberts, H.J., 2010. A High-Resolution
1095 Coupled Riverine Flow, Tide, Wind, Wind Wave, and Storm Surge Model for Southern Louisiana and Mississippi.
1096 Part I: Model Development and Validation. <https://doi.org/10.1175/2009MWR2906.1>

1097 Cangialosi, J.P., Latta, A.S., Berg, R., 2018. Tropical cyclone report: hurricane Irma. National Hurricane Center, Miami.

1098 CGEDD, 2010. Tempête Xynthia: Retour d’expérience, évaluation et propositions d’action.

1099 Consortium EMODnet Bathymetry, 2018. EMODnet Digital Bathymetry (DTM) [WWW Document]. URL
1100 <https://sextant.ifremer.fr/record/18ff0d48-b203-4a65-94a9-5fd8b0ec35f6/> (accessed 6.21.22).

1101 DDTM, 2011. Éléments de mémoire sur la tempête Xynthia du 27 et 28 février 2010 [WWW Document]. Serv. L’État En
1102 Charente-Marit. URL <https://www.charente-maritime.gouv.fr/Actions-de-l-Etat/Environnement-risques-naturels-et-technologiques/Risques-naturels-et-technologiques/Generalites-sur-la-prevention-des-risques-naturels/Elements-de-memoire-Xynthia/Elements-de-memoire-sur-la-tempete-Xynthia-du-27-et-28-fevrier-2010> (accessed 9.16.24).

1103

1104

1105 Deltares, 2024. D-Flow Flexible Mesh User Manual.

1106 Deltares, 2021. Model description and development - Global Tide and Surge Model - Deltares Public Wiki [WWW
1107 Document]. URL <https://publicwiki.deltares.nl/display/GTSM/Model+description+and+development> (accessed
1108 10.7.24).

1109 Dietrich, J.C., Bunya, S., Westerink, J.J., Ebersole, B.A., Smith, J.M., Atkinson, J.H., Jensen, R., Resio, D.T., Luettich, R.A.,
1110 Dawson, C., Cardone, V.J., Cox, A.T., Powell, M.D., Westerink, H.J., Roberts, H.J., 2010. A High-Resolution
1111 Coupled Riverine Flow, Tide, Wind, Wind Wave, and Storm Surge Model for Southern Louisiana and Mississippi.
1112 Part II: Synoptic Description and Analysis of Hurricanes Katrina and Rita.
1113 <https://doi.org/10.1175/2009MWR2907.1>

1114 Douris, J., Kim, G., Abrahams, J., Lapitan Moreno, J., Shumake-Guillemot, J., Green, H., Murray, V., 2021. WMO Atlas of
1115 Mortality and Economic Losses from Weather, Climate and Water Extremes (1970–2019) (WMO-No. 1267),
1116 WMO. WMO, Geneva.

1117 Dullaart, J.C.M., Muis, S., Bloemendaal, N., Aerts, J.C.J.H., 2020. Advancing global storm surge modelling using the new
1118 ERA5 climate reanalysis. *Clim. Dyn.* 54, 1007–1021. <https://doi.org/10.1007/s00382-019-05044-0>

1119 Dullaart, J.C.M., Muis, S., Bloemendaal, N., Chertova, M.V., Couasnon, A., Aerts, J.C.J.H., 2021. Accounting for tropical
1120 cyclones more than doubles the global population exposed to low-probability coastal flooding. *Commun. Earth
1121 Environ.* 2, 1–11. <https://doi.org/10.1038/s43247-021-00204-9>

1122 Eilander, D., Couasnon, A., Ikeuchi, H., Muis, S., Yamazaki, D., Winsemius, H.C., Ward, P.J., 2020. The effect of surge on
1123 riverine flood hazard and impact in deltas globally. *Environ. Res. Lett.* 15. [https://doi.org/10.1088/1748-](https://doi.org/10.1088/1748-9326/ab8ca6)
1124 [9326/ab8ca6](https://doi.org/10.1088/1748-9326/ab8ca6)

1125 Eilander, D., Couasnon, A., Leijnse, T., Ikeuchi, H., Yamazaki, D., Muis, S., Dullaart, J., Haag, A., Winsemius, H.C., Ward,
1126 P.J., 2023. A globally applicable framework for compound flood hazard modeling. *Nat. Hazards Earth Syst. Sci.* 23,
1127 823–846. <https://doi.org/10.5194/nhess-23-823-2023>

1128 Emanuel, K., Rotunno, R., 2011. Self-Stratification of Tropical Cyclone Outflow. Part I: Implications for Storm Structure.
1129 <https://doi.org/10.1175/JAS-D-10-05024.1>

1130 GEBCO, 2014. General Bathymetric Chart of the Oceans (GEBCO) 2014 Grid [WWW Document]. URL
1131 <https://www.gebco.net/> (accessed 6.21.22).

1132 Haigh, I.D., Marcos, M., Talke, S.A., Woodworth, P.L., Hunter, J.R., Hague, B.S., Ams, A., Bradshaw, E., Thompson, P.,
1133 2023. GESLA Version 3: A major update to the global higher-frequency sea-level dataset. *Geosci. Data J.* 10, 293–
1134 314. <https://doi.org/10.1002/gdj3.174>

1135 Haigh, I.D., Wadey, M.P., Wahl, T., Ozsoy, O., Nicholls, R.J., Brown, J.M., Horsburgh, K., Gouldby, B., 2016. Spatial and
1136 temporal analysis of extreme sea level and storm surge events around the coastline of the UK. *Sci. Data* 3, 1–14.
1137 <https://doi.org/10.1038/sdata.2016.107>

1138 Harper, B.A., Kepert, J.D., Ginger, J.D., 2010. Guidelines for Converting Between Various Wind Averaging Periods in
1139 Tropical Cyclone Conditions. WMO.

1140 Hawker, L., Uhe, P., Paulo, L., Sosa, J., Savage, J., Sampson, C., Neal, J., 2022. A 30 m global map of elevation with forest s
1141 and buildings removed. *Environ. Res. Lett.* 17, 024016. <https://doi.org/10.1088/1748-9326/ac4d4f>

1142 Hersbach, H., Bell, B., Berrisford, P., Horányi, A., Sabater, J.M., Nicolas, J., Radu, R., Schepers, D., Simmons, A., Soci, C.,
1143 Dee, D., 2019. Global reanalysis: goodbye ERA-Interim, hello ERA5. *ECMWF Newsl.* 17–24.
1144 <https://doi.org/10.21957/vf291hehd7>

1145 Hinkel, J., Lincke, D., Vafeidis, A.T., Perrette, M., Nicholls, R.J., Tol, R.S.J., Marzeion, B., Fettweis, X., Ionescu, C.,
1146 Levermann, A., 2014. Coastal flood damage and adaptation costs under 21st century sea-level rise. *Proc. Natl.*
1147 *Acad. Sci.* 111, 3292–3297. <https://doi.org/10.1073/pnas.1222469111>

1148 Holland, G.J., Belanger, J.I., Fritz, A., 2010. A revised model for radial profiles of hurricane winds. *Mon. Weather Rev.* 138,
1149 4393–4401. <https://doi.org/10.1175/2010MWR3317.1>

1150 Hu, K., Chen, Q., Kimball, S.K., 2011. Consistency in hurricane surface wind forecasting: an improved parametric model.
1151 *Nat. Hazards* 61, 1029–1050. <https://doi.org/10.1007/s11069-011-9960-z>

1152 Kemkamp, H.W.J., Van Dam, A., Stelling, G.S., de Goede, E.D., 2011. Efficient scheme for the shallow water equations on
1153 unstructured grids with application to the Continental Shelf. *Ocean Dyn.* 61, 1175–1188.
1154 <https://doi.org/10.1007/s10236-011-0423-6>

1155 Kirezci, E., Young, I.R., Ranasinghe, R., Muis, S., Nicholls, R.J., Lincke, D., Hinkel, J., 2020. Projections of global-scale
1156 extreme sea levels and resulting episodic coastal flooding over the 21st Century. *Sci. Rep.* 10, 1–12.
1157 <https://doi.org/10.1038/s41598-020-67736-6>

1158 Lapidez, J.P., Tablazon, J., Dasallas, L., Gonzalo, L.A., Cabacaba, K.M., Ramos, M.M.A., Suarez, J.K., Santiago, J.,
1159 Lagmay, A.M.F., Malano, V., 2015. Identification of storm surge vulnerable areas in the Philippines through the
1160 simulation of Typhoon Haiyan-induced storm surge levels over historical storm tracks. *Hazards Earth Syst Sci* 15,
1161 1473–1481. <https://doi.org/10.5194/nhess-15-1473-2015>

1162 Leijnse, T., Nederhoff, K., Van Dongeren, A., McCall, R.T., Van Ormondt, M., 2020. Improving Computational Efficiency
1163 of Compound Flooding Simulations: the SFINCS Model with Subgrid Features 2020, NH022-0006.

- 1164 Leijnse, T., Van Ormondt, M., Nederhoff, K., Van Dongeren, A., 2021. Modeling compound flooding in coastal systems
1165 using a computationally efficient reduced-physics solver: Including fluvial, pluvial, tidal, wind- and wave-driven
1166 processes. *Coast. Eng.* 163, 103796. <https://doi.org/10.1016/j.coastaleng.2020.103796>
- 1167 Lin, N., Chavas, D., 2012. On hurricane parametric wind and applications in storm surge modeling. *J. Geophys. Res.*
1168 *Atmospheres* 117, 1–19. <https://doi.org/10.1029/2011JD017126>
- 1169 Marcos, M., Rohmer, J., Vousdoukas, M.I., Mentaschi, L., Le Cozannet, G., Amores, A., 2019. Increased Extreme Coastal
1170 Water Levels Due to the Combined Action of Storm Surges and Wind Waves. *Geophys. Res. Lett.* 46, 4356–4364.
1171 <https://doi.org/10.1029/2019GL082599>
- 1172 Mori, N., Kato, M., Kim, S., Mase, H., Shibutani, Y., Takemi, T., Tsuboki, K., Yasuda, T., 2014. Local amplification of
1173 storm surge by Super Typhoon Haiyan in Leyte Gulf. *Geophys. Res. Lett.* 41, 5106–5113.
1174 <https://doi.org/10.1002/2014GL060689>
- 1175 Muis, S., Apecechea, M.I., Dullaart, J., de Lima Rego, J., Madsen, K.S., Su, J., Yan, K., Verlaan, M., 2020. A High -
1176 Resolution Global Dataset of Extreme Sea Levels, Tides, and Storm Surges, Including Future Projections. *Front.*
1177 *Mar. Sci.* 7, 1–15. <https://doi.org/10.3389/fmars.2020.00263>
- 1178 Muis, S., Verlaan, M., Winsemius, H.C., Aerts, J.C.J.H., Ward, P.J., 2016. A global reanalysis of storm surges and extreme
1179 sea levels. *Nat. Commun.* 7, 11969. <https://doi.org/10.1038/ncomms11969>
- 1180 Naval Meteorology and Oceanography Command, 2022. Naval Oceanography Portal, Best Track Archive [WWW
1181 Document]. URL <https://www.metoc.navy.mil/jtwc/jtwc.html?best-tracks> (accessed 10.10.24).
- 1182 Nhamo, G., Chikodzi, D., 2021. Cyclones in Southern Africa: Volume 1: Interfacing the Catastrophic Impact of Cyclone Idai
1183 with SDGs in Zimbabwe, Sustainable Development Goals Series. Springer International Publishing, Cham.
1184 <https://doi.org/10.1007/978-3-030-72393-4>
- 1185 Pelupessy, I., Van Werkhoven, B., Van Elteren, A., Viebahn, J., Candy, A., Zwart, S.P., Dijkstra, H., 2017. The
1186 Oceanographic Multipurpose Software Environment (OMUSE v1.0). *Geosci. Model Dev.* 10, 3167–3187.
1187 <https://doi.org/10.5194/gmd-10-3167-2017>
- 1188 Pringle, W.J., Wirasaet, D., Roberts, K.J., Westerink, J.J., 2021. Global storm tide modeling with ADCIRC v55:
1189 unstructured mesh design and performance. *Geosci. Model Dev.* 14, 1125–1145. <https://doi.org/10.5194/gmd-14-1125-2021>
- 1191 Ramirez, J.A., Lichter, M., Coulthard, T.J., Skinner, C., 2016. Hyper-resolution mapping of regional storm surge and tide
1192 flooding: comparison of static and dynamic models. *Nat. Hazards* 82, 571–590. <https://doi.org/10.1007/s11069-016-2198-z>
- 1194 Sebastian, A., Bader, D.J., Nederhoff, C.M., Leijnse, T.W.B., Bricker, J.D., Aarninkhof, S.G.J., 2021. Hindcast of pluvial,
1195 fluvial, and coastal flood damage in Houston, Texas during Hurricane Harvey (2017) using SFINCS. *Nat. Hazards*.
1196 <https://doi.org/10.1007/s11069-021-04922-3>
- 1197 Tiggeloven, T., De Moel, H., Winsemius, H.C., Eilander, D., Erkens, G., Gebremedhin, E., Diaz Loaiza, A., Kuzma, S., Luo,
1198 T., Iceland, C., Bouwman, A., Van Huijstee, J., Ligtvoet, W., Ward, P.J., 2020. Global-scale benefit-cost analysis of
1199 coastal flood adaptation to different flood risk drivers using structural measures. *Nat. Hazards Earth Syst. Sci.* 20,
1200 1025–1044. <https://doi.org/10.5194/nhess-20-1025-2020>
- 1201 UNDRR, 2020. The human cost of disasters: an overview of the last 20 years (2000-2019) | UNDRR [WWW Document].
1202 URL <https://www.undrr.org/publication/human-cost-disasters-overview-last-20-years-2000-2019> (accessed
1203 9.27.22).
- 1204 Vafeidis, A.T., Schuerch, M., Wolff, C., Spencer, T., Merkens, J.L., Hinkel, J., Lincke, D., Brown, S., Nicholls, R.J., 2019.
1205 Water-level attenuation in global-scale assessments of exposure to coastal flooding: A sensitivity analysis. *Nat.*
1206 *Hazards Earth Syst. Sci.* 19, 973–984. <https://doi.org/10.5194/nhess-19-973-2019>

1207 Veenstra, J., 2024. *dfm_tools*: A Python package for pre- and postprocessing D-FlowFM model input and output files.
1208 <https://doi.org/10.5281/zenodo.10633862>

1209 Vitousek, S., Barnard, P.L., Fletcher, C.H., Frazer, N., Erikson, L., Storlazzi, C.D., 2017. Doubling of coastal flooding
1210 frequency within decades due to sea-level rise. *Sci. Rep.* 7, 1–9. <https://doi.org/10.1038/s41598-017-01362-7>

1211 Vousdoukas, M.I., Bouziotas, D., Giardino, A., Bouwer, L.M., Mentaschi, L., Voukouvalas, E., Feyen, L., 2018a.
1212 Understanding epistemic uncertainty in large-scale coastal flood risk assessment for present and future climates.
1213 *Nat. Hazards Earth Syst. Sci.* 18, 2127–2142. <https://doi.org/10.5194/nhess-18-2127-2018>

1214 Vousdoukas, M.I., Mentaschi, L., Voukouvalas, E., Verlaan, M., Feyen, L., 2017. Extreme sea levels on the rise along
1215 Europe’s coasts. *Earths Future* 5, 304–323. <https://doi.org/10.1002/2016EF000505>

1216 Vousdoukas, M.I., Mentaschi, L., Voukouvalas, E., Verlaan, M., Jevrejeva, S., Jackson, L.P., Feyen, L., 2018b. Global
1217 probabilistic projections of extreme sea levels show intensification of coastal flood hazard. *Nat. Commun.* 9, 1–12.
1218 <https://doi.org/10.1038/s41467-018-04692-w>

1219 Vousdoukas, M.I., Voukouvalas, E., Annunziato, A., Giardino, A., Feyen, L., 2016a. Projections of extreme storm surge
1220 levels along Europe. *Clim. Dyn.* 47, 3171–3190. <https://doi.org/10.1007/s00382-016-3019-5>

1221 Vousdoukas, M.I., Voukouvalas, E., Mentaschi, L., Dottori, F., Giardino, A., Bouziotas, D., Bianchi, A., Salamon, P., Feyen,
1222 L., 2016b. Developments in large-scale coastal flood hazard mapping. *Nat. Hazards Earth Syst. Sci.* 16, 1841–1853.
1223 <https://doi.org/10.5194/nhess-16-1841-2016>

1224 Wadey, M.P., Haigh, I.D., Nicholls, R.J., Brown, J.M., Horsburgh, K., Carroll, B., Gallop, S.L., Mason, T., Bradshaw, E.,
1225 2015. A comparison of the 31 January–1 February 1953 and 5–6 December 2013 coastal flood events around the
1226 UK. *Front. Mar. Sci.* 2. <https://doi.org/10.3389/fmars.2015.00084>

1227 Wahl, T., 2017. Sea-level rise and storm surges, relationship status: Complicated! *Environ. Res. Lett.* 12.
1228 <https://doi.org/10.1088/1748-9326/aa8eba>

1229 Wahl, T., Haigh, I.D., Nicholls, R.J., Arns, A., Dangendorf, S., Hinkel, J., Slangen, A.B.A., 2017. Understanding extreme
1230 sea levels for broad-scale coastal impact and adaptation analysis. *Nat. Commun.* 8, 1–12.
1231 <https://doi.org/10.1038/ncomms16075>

1232 Wang, P., Bernier, N.B., 2023. Adding sea ice effects to a global operational model (NEMO v3.6) for forecasting total water
1233 level: approach and impact. *Geosci. Model Dev.* 16, 3335–3354. <https://doi.org/10.5194/gmd-16-3335-2023>

1234 Wang, X., Verlaan, M., Apecechea, M.I., Lin, H.X., 2022. Parameter estimation for a global tide and surge model with a
1235 memory-efficient order reduction approach. *Ocean Model.* 173, 102011.
1236 <https://doi.org/10.1016/j.ocemod.2022.102011>

1237 Ward, P.J., Blauhut, V., Bloemendaal, N., Daniell, E.J., De Ruiter, C.M., Duncan, J.M., Emberson, R., Jenkins, F.S.,
1238 Kirschbaum, D., Kunz, M., Mohr, S., Muis, S., Riddell, A.G., Schäfer, A., Stanley, T., Veldkamp, I.E.T., Hessel,
1239 W.C., 2020. Review article: Natural hazard risk assessments at the global scale. *Nat. Hazards Earth Syst. Sci.* 20,
1240 1069–1096. <https://doi.org/10.5194/nhess-20-1069-2020>

1241 Weatherall, P., Tozer, B., Arndt, J.E., Bazhenova, E., Bringensparr, C., Castro, C., Dorschel, B., Ferrini, V., Hehemann, L.,
1242 Jakobsson, M., Johnson, P., Ketter, T., Mackay, K., Martin, T., McMichael-Phillips, J., Mohammad, R., Nitsche, F.,
1243 Sandwell, D., Viquerat, S., 2020. The GEBCO_2020 Grid - a continuous terrain model of the global oceans and
1244 land. <https://doi.org/10.5285/a29c5465-b138-234d-e053-6c86abc040b9>

1245 Woodruff, J., Dietrich, J.C., Wirsaet, D., Kennedy, A.B., Bolster, D., 2023. Storm surge predictions from ocean to subgrid
1246 scales. *Nat. Hazards* 117, 2989–3019. <https://doi.org/10.1007/s11069-023-05975-2>

1247

1248 **Acknowledgements**

1249 This work was carried out in the EU-ERC COASTMOVE project nr 884442 and the NWO MOSAIC project nr
1250 ASDI.2018.036. The authors would like to thank the SURF Cooperative for the support in using the Dutch national e-
1251 infrastructure under grant no. EINF-2224 and EINF-5779.

1252 **Author contributions**

1253 I.B.: Conceptualisation, Investigation, Methodology, Modelling, Visualisation, Analysis, Writing – Original Draft. J.C.J.H.A.:
1254 Conceptualisation, Investigation, Methodology, Writing – Review & Editing, Supervision. P.J.W.: Conceptualisation,
1255 Investigation, Methodology, Writing – Review & Editing, Supervision. D.E.: Conceptualisation, Investigation, Methodology,
1256 Modelling, Writing – Review & Editing, Supervision. S.M.: Conceptualisation, Investigation, Methodology, Modelling,
1257 Writing – Review & Editing, Supervision.

1258 **Competing interests**

1259 One of the (co-)authors is a member of the editorial board of Natural Hazards and Earth System Sciences.